ACCURACY IMPROVEMENT OF THE SECOND-KIND FREDHOLM INTEGRAL EQUATIONS IN COMPUTATIONAL ELECTROMAGNETICS

BY

SU YAN

THESIS

Submitted in partial fulfillment of the requirements
for the degree of Master of Science in Electrical and Computer Engineering
in the Graduate College of the
University of Illinois at Urbana-Champaign, 2012

Urbana, Illinois

Adviser:

Professor Jianming Jin

ABSTRACT

In computational electromagnetics, the second-kind Fredholm integral equations (IEs) are known to have very fast iterative convergence but rather poor solution accuracy compared with the first-kind Fredholm integral equations. The loss of the numerical accuracy is mainly due to the discretization error of the identity operators involved in second-kind IEs. In the past decade, although much effort has been made to improve the numerical accuracy of the second-kind integral equations, no conclusive understandings and final resolutions are achieved.

In this thesis, the widely used surface integral equations in computational electromagnetics are first presented along with the discussions of their respective mathematical and numerical properties. The integral operators involved in these integral equations are investigated in terms of their mathematical properties and numerical discretization strategies. Based on such discussions and investigations, a numerical scheme is presented to significantly suppress the discretization error of the identity operators by using the Buffa-Christiansen (BC) functions as the testing function, leading to much more accurate solutions to the second-kind integral equations for smooth objects in both perfect electric conductor (PEC) and dielectric cases, while maintaining their fast convergence properties. This technique is then generalized for generally shaped objects in both PEC and dielectric cases by using the BC functions as the testing functions, and by handling the near-singularities in the evaluation of the system matrix elements carefully. The extinction theorem is applied for accurate evaluation of the numerical errors in the calculation of scattering problems for generally shaped objects. Several examples are given to investigate and demonstrate the performance of the proposed techniques in the accuracy improvement of the second-kind surface integral equations in both PEC and dielectric cases. The reasons for the accuracy improvement are explained, and several important conclusive remarks are made.

To my parents and my wife, for their love and support

ACKNOWLEDGMENTS

On the completion of this thesis, I would like to express my cordial gratitude to my graduate adviser, Professor Jian-Ming Jin, without whom I would not have been able to complete this work. During my study at the University of Illinois at Urbana-Champaign (UIUC), Professor Jin has provided me with his advice, support, and encouragement, from which I have benefited a lot.

I would like to thank every current and former member in Professor Jin's research group at UIUC for their friendship and their helpful discussions and suggestions.

Finally, I want to give my sincere gratitude to my parents and my wife, Xiuling Zhu, for their dedication and their continued love and support.

TABLE OF CONTENTS

CHAPTER 1

INTRODUCTION

Surface integral equations (SIEs) are very widely used in modeling electromagnetic scattering and radiation problems involving perfect electric conductors (PECs) and dielectric objects. Obtained by using dyadic Green's functions [1] as the integral kernels and integrating over the entire surfaces of the objects under consideration, SIEs can be categorized into the Fredholm integral equations [2] of the first and the second kinds. In computational electromagnetics, the first-kind Fredholm integral equations, or the homogeneous Fredholm integral equations, are known to have very good accuracy, but rather poor convergence in an iterative solution because of their unbounded integral operators, which produce system matrices with large condition numbers after discretization. In contrast, the second-kind Fredholm integral equations, or the inhomogeneous Fredholm integral equations, usually have a fast convergence rate in an iterative solution since they are in the form of an identity operator plus a compact integral operator. A compact operator, in functional analysis, is a linear operator transforming from a Banach space $\mathscr{D}$ to another Banach space $\mathscr{R}$, such that the image of any bounded subset of $\mathscr{D}$ under the operator is a relatively compact subset of $\mathscr{R}$. Such an operator is a well-bounded operator, and produces a system matrix with eigenvalues clustered around zero. Consequently, the second-kind Fredholm integral equations give rise to the system matrices that have bounded eigenvalues clustered around a non-zero point, which makes the matrices very well-conditioned. However, the second-kind integral equations have a drawback in that their solutions are far less accurate than their first-kind counterparts; therefore, they are less commonly used for practical applications.

In computational electromagnetics, the first-kind integral equations include the electric-field integral equation (EFIE) [3] for the PEC case and the Poggio-Miller-Chang-Harrington-Wu-Tsai (PMCHWT) equations [4–7]

for the dielectric case, while the second-kind integral equations include the magnetic-field integral equation (MFIE) [3] for the PEC case and the Müller equations [8–10] for the dielectric case. In recent years, much effort has been devoted to improving the accuracy of the second-kind Fredholm integral equations, especially the MFIE for the PEC case. Most of these efforts focus on the accuracy loss caused by the integral operation [11–21]. Among these studies, some attributed the inaccuracy of the MFIE to the inaccurate evaluation of the impedance elements [11–13], including the logarithmic singularity in the field integration [14, 15], and the solid angle expression in the MFIE formulation [16]. Some believed that the inappropriate choice of the basis functions caused the problem [17], and hence, proposed the use of the linear-linear basis functions [18, 19] and higher-order vector basis functions [20] to alleviate this problem. Some showed that the improperly chosen solution scheme is another important error source, and proposed the Rayleigh-Ritz scheme for the three-dimensional MFIE to alleviate this error [21].

Other research efforts have investigated the error caused by the identity operator in the MFIE. It has been shown that there is actually a large discretization error due to the identity operator [22], which contributes significantly to the total error of the MFIE. In order to alleviate the accuracy loss caused by the identity operator, regularization methods have been proposed for both two-dimensional [23] and three-dimensional [24] cases. The basic idea is to design a "filter" to filter out the high-frequency content in the basis functions and to increase their effective smoothness. Such "filtering", unfortunately, is not easily applicable to the three-dimensional case. As a result, the regularization method in the three-dimensional case is not as effective as its two-dimensional counterpart. More recently, a rotated Buffa-Christiansen (BC) function [25] is adopted as the testing function in the discretization of the MFIE in order to achieve a better accuracy [26]. However, the use of planar patches limits the improvement of the accuracy. Moreover, the limitation of discussion of the second-kind integral equation to the PEC case and the lack of mathematical and numerical explanation of the accuracy improvement also limit its significance. In sum, with all these methods, the accuracy of the MFIE solution is still worse than that of the EFIE solution. Therefore, the EFIE is always preferred over the MFIE in the analysis of electromagnetic scattering and radiation by a PEC object, especially when accuracy is important.

Although much more complicated, a similar issue has been observed in the dielectric case, where the PMCHWT equations [4–7] are the Fredholm integral equations of the first kind and the Müller equations [8–10] are the Fredholm integral equations of the second kind. Their convergence behavior in an iterative solution and the solution accuracy have been investigated thoroughly [20] and the first-kind equations (PMCHWT equations) have been shown to always have a better accuracy and a worse convergence compared to the second-kind equations (Müller equations). Hence, the PMCHWT equations are always preferred for an accurate solution of electromagnetic scattering and radiation by a dielectric object.

Although the accuracy issue of the second-kind integral equations has been studied for more than a decade, no conclusive understandings and final resolutions are achieved [27].

In this thesis, the SIEs for both PEC and dielectric cases are first presented, and the discretization schemes for different integral operators are discussed. The discretization error due to the identity operator is then suppressed by using the rotated BC functions defined on curvilinear triangular patches [28] as the testing function. It is demonstrated through several numerical examples that the accuracy of the second-kind Fredholm integral equations (the MFIE and Müller equations), in both PEC and dielectric cases, can be improved significantly using this discretization scheme for smooth objects.

The accuracy improvement technique is then generalized to the solution of electromagnetic problems with generally shaped objects in both the PEC and the dielectric cases. By using the BC functions as the testing functions and by carefully handling the near-singularities associated with both the $\mathcal{K}$ and the $\mathcal{T}$ operators, the numerical accuracy of the second-kind integral equations in the solution to a generally shaped object can be improved significantly. In order to measure the numerical error in solving problems with generally shaped objects, null-field problems are presented according to the extinction theorem, and the root-mean-square (RMS) error of the total field in the far-zone is defined as the numerical error in the solutions of the integral equations. Several numerical examples are given to demonstrate the performance of the proposed techniques in improving the numerical accuracy of the second-kind integral equations.

Before the conclusion is drawn, the reasons for the accuracy improvement of the proposed scheme are discussed and attributed to the significant sup-

pression of the discretization error of the identity operator and the appropriate adoption of the Rayleigh-Ritz scheme [21]; the improvement is also explained in terms of the method of weighted residuals [29] and the accurate evaluation of the near-singularities. Some important conclusive remarks are also given to clarify several important issues related to the accuracy of the integral equations.

CHAPTER 2

SURFACE INTEGRAL EQUATIONS

In this chapter, the general formulations for electromagnetic problems are first reviewed. The SIEs for both PEC and dielectric cases are then presented. Discussion shows how these SIEs can be categorized into the Fredholm integral equations of the first and second kinds.

2.1 General Formulations

In this section, the electromagnetic problem is first formulated in a general way where multiple excitations are considered in the physical model. The problem is then simplified into two special cases in the next section, and the discussions will be made for each case.

Consider an electromagnetic problem with the incident plane wave ($\boldsymbol{E}_1^{\text{inc}}$, $\boldsymbol{H}_1^{\text{inc}}$) coming from an infinite homogeneous background medium Ω_1 with permittivity ε_1 and permeability μ_1, and illuminating a homogeneous object Ω_2 with permittivity ε_2 and permeability μ_2. In the meantime, a second incident wave ($\boldsymbol{E}_2^{\text{inc}}$, $\boldsymbol{H}_2^{\text{inc}}$) comes from the interior of Ω_2, and illuminates the object from inside out. According to the surface equivalence principle [30,31], the solution can be formulated in terms of an equivalent surface electric current $\boldsymbol{J} = \hat{\boldsymbol{n}} \times \boldsymbol{H}_1^{\text{tol}} = \hat{\boldsymbol{n}} \times \boldsymbol{H}_2^{\text{tol}}$ and an equivalent surface magnetic current $\boldsymbol{M} = \boldsymbol{E}_1^{\text{tol}} \times \hat{\boldsymbol{n}} = \boldsymbol{E}_2^{\text{tol}} \times \hat{\boldsymbol{n}}$ defined on the surface S of the object. Here, $\hat{\boldsymbol{n}}$ stands for the outward pointing unit normal vector on S, $\boldsymbol{E}_j^{\text{tol}}$ and $\boldsymbol{H}_j^{\text{tol}}$ stand for the total electric and magnetic fields in Ω_j $(j = 1, 2)$, respectively. The equivalent surface currents are governed by the EFIEs

$$\mathcal{T}_1 (\eta_1 \boldsymbol{J}) + \left[\frac{\mathcal{I}}{2} - \mathcal{K}_1 \right] (\boldsymbol{M}) = -\hat{\boldsymbol{n}} \times \boldsymbol{E}_1^{\text{inc}} \tag{2.1}$$

$$\frac{\eta_2}{\eta_1} \mathcal{T}_2 (\eta_1 \boldsymbol{J}) - \left[\frac{\mathcal{I}}{2} + \mathcal{K}_2 \right] (\boldsymbol{M}) = \hat{\boldsymbol{n}} \times \boldsymbol{E}_2^{\text{inc}} \tag{2.2}$$

which can be written in a matrix form as

$$\begin{bmatrix} \mathcal{T}_1 & \dfrac{\mathcal{I}}{2}-\mathcal{K}_1 \\ \dfrac{\eta_2}{\eta_1}\mathcal{T}_2 & -\dfrac{\mathcal{I}}{2}-\mathcal{K}_2 \end{bmatrix} \begin{bmatrix} \eta_1\boldsymbol{J} \\ \boldsymbol{M} \end{bmatrix} = \begin{bmatrix} -\hat{\boldsymbol{n}}\times\boldsymbol{E}_1^{\text{inc}} \\ \hat{\boldsymbol{n}}\times\boldsymbol{E}_2^{\text{inc}} \end{bmatrix} \tag{2.3}$$

and the MFIEs

$$\left[-\frac{\mathcal{I}}{2}+\mathcal{K}_1\right](\eta_1\boldsymbol{J})+\mathcal{T}_1(\boldsymbol{M}) = -\eta_1\hat{\boldsymbol{n}}\times\boldsymbol{H}_1^{\text{inc}} \tag{2.4}$$

$$\left[\frac{\mathcal{I}}{2}+\mathcal{K}_2\right](\eta_1\boldsymbol{J})+\frac{\eta_1}{\eta_2}\mathcal{T}_2(\boldsymbol{M}) = \eta_1\hat{\boldsymbol{n}}\times\boldsymbol{H}_2^{\text{inc}} \tag{2.5}$$

which can be written in a matrix form as

$$\begin{bmatrix} -\dfrac{\mathcal{I}}{2}+\mathcal{K}_1 & \mathcal{T}_1 \\ \dfrac{\mathcal{I}}{2}+\mathcal{K}_2 & \dfrac{\eta_1}{\eta_2}\mathcal{T}_2 \end{bmatrix} \begin{bmatrix} \eta_1\boldsymbol{J} \\ \boldsymbol{M} \end{bmatrix} = \begin{bmatrix} -\eta_1\hat{\boldsymbol{n}}\times\boldsymbol{H}_1^{\text{inc}} \\ \eta_1\hat{\boldsymbol{n}}\times\boldsymbol{H}_2^{\text{inc}} \end{bmatrix} \tag{2.6}$$

where $\eta_j{=}\sqrt{\mu_j/\varepsilon_j}$ stands for the intrinsic impedance in Ω_j $(j{=}1,2)$, $\mathcal{I}$ stands for the identity operator, and $\mathcal{T}_j$ and $\mathcal{K}_j$ are the integral operators defined as

$$\mathcal{T}_j(\boldsymbol{X}){=}ik_j\hat{\boldsymbol{n}}\times\int_{S'}\left(\mathcal{I}+\frac{\nabla\nabla}{k_j^2}\right)G(\boldsymbol{r},\boldsymbol{r}';k_j)\cdot\boldsymbol{X}(\boldsymbol{r}')\mathrm{d}\boldsymbol{r}' \tag{2.7}$$

$$\mathcal{K}_j(\boldsymbol{X}){=}\hat{\boldsymbol{n}}\times P.V.\int_{S'}\nabla G(\boldsymbol{r},\boldsymbol{r}';k_j)\times\boldsymbol{X}(\boldsymbol{r}')\mathrm{d}\boldsymbol{r}'. \tag{2.8}$$

In the above, k_j stands for the wavenumber in Ω_j, $G(\boldsymbol{r},\boldsymbol{r}';k_j)=e^{ik_j|\boldsymbol{r}-\boldsymbol{r}'|}/4\pi|\boldsymbol{r}-\boldsymbol{r}'|$ stands for the Green's function in an infinite homogeneous medium with the wavenumber k_j, and $\boldsymbol{X}$ stands for either the scaled surface electric current density $\eta_1\boldsymbol{J}$ or the surface magnetic current density $\boldsymbol{M}$. In (2.8), $P.V.$ stands for the Cauchy principal value integration. In (2.1)-(2.6), $\eta_1\boldsymbol{J}$ instead of $\boldsymbol{J}$ is treated as the unknown function and η_1 is multiplied on (2.4) and (2.5) in order to balance the magnitude of each operator in the above equations and make the whole system better conditioned. Equations (2.1) and (2.4) are derived from the formulation of the exterior fields in Ω_1, and (2.2) and (2.5) are derived from the formulation of the interior fields in Ω_2. Applying (2.1) to (2.6) to different scatterers with different boundary conditions, we can obtain various SIEs.

2.1.1 SIEs in the PEC Case

If the obstruction is a PEC object, the application of the boundary condition $\hat{\boldsymbol{n}} \times \boldsymbol{E} = 0$ results in $\boldsymbol{M} = 0$, which, when substituted into (2.1)-(2.2) and (2.4)-(2.5), yields the EFIE for the PEC case as

$$\mathcal{T}_1 (\eta_1 \boldsymbol{J}) = -\hat{\boldsymbol{n}} \times \boldsymbol{E}_1^{\text{inc}} \tag{2.9}$$

$$\mathcal{T}_2 (\eta_2 \boldsymbol{J}) = \hat{\boldsymbol{n}} \times \boldsymbol{E}_2^{\text{inc}} \tag{2.10}$$

and the MFIE for the PEC case as

$$-\frac{\eta_1 \boldsymbol{J}}{2} + \mathcal{K}_1 (\eta_1 \boldsymbol{J}) = -\eta_1 \hat{\boldsymbol{n}} \times \boldsymbol{H}_1^{\text{inc}} \tag{2.11}$$

$$-\frac{\eta_2 \boldsymbol{J}}{2} - \mathcal{K}_2 (\eta_2 \boldsymbol{J}) = -\eta_2 \hat{\boldsymbol{n}} \times \boldsymbol{H}_2^{\text{inc}}. \tag{2.12}$$

Although both the EFIE (2.9), (2.10) and the MFIE (2.11), (2.12) can be solved independently to obtain the equivalent electric current density $\boldsymbol{J}$, they suffer from the "interior resonance corruption" [32] at some discrete frequencies. As a remedy, their convex combination, the combined-field integral equation (CFIE) [3], can be used. For example,

$$\begin{aligned} &\left[\alpha\, \hat{\boldsymbol{n}} \times \mathcal{T}_1 + (1-\alpha) \left(-\frac{\mathcal{I}}{2} + \mathcal{K}_1\right)\right] (\eta_1 \boldsymbol{J}) \\ &= -\alpha\, \hat{\boldsymbol{n}} \times \hat{\boldsymbol{n}} \times \boldsymbol{E}_1^{\text{inc}} - (1-\alpha)\, \eta_1 \hat{\boldsymbol{n}} \times \boldsymbol{H}_1^{\text{inc}} \end{aligned} \tag{2.13}$$

where $\alpha \in [\,0, 1\,]$ is a linear combination factor.

As has been studied extensively [20,33], the $\mathcal{T}$ operator is a Fredholm integral operator of the first kind, which has a continuous spectrum distribution (and the corresponding discrete eigenvalue distribution after discretization) clustering at origin and infinity, resulting in an unbounded condition number that approaches infinity when the discretization density is increasingly refined. However, because of its high accuracy and the capability to handle objects with open surfaces, the EFIE is still widely used whenever possible. On the other hand, since the $\mathcal{K}$ operator is a compact operator, the whole MFIE operator is actually an identity operator plus a compact operator, which makes the MFIE a Fredholm integral equation of the second kind. As mentioned above, the MFIE has a very good iterative convergence but a rather poor solution accuracy, and therefore is less commonly used than the

EFIE. As their combination, the CFIE inherits the characteristics from both the EFIE and the MFIE. Hence, it has a better iterative convergence but a worse solution accuracy [34] compared with the EFIE, and its performance depends on the choice of the combination factor α.

2.1.2 SIEs in the Dielectric Case

If the obstruction is a dielectric object, by solving either (2.3) or (2.6), we can obtain the solution of the scattering problem. However, since both (2.3) and (2.6) suffer from the interior resonance corruption, their combinations are usually used. One approach is to combine (2.1) with (2.4) to form a CFIE for the exterior region Ω_1, and combine (2.2) with (2.5) to form a CFIE for the interior region Ω_2. These two equations then form a complete system that can be solved for $\boldsymbol{J}$ and $\boldsymbol{M}$ [35]. Another approach is to combine (2.1) with (2.2) and (2.4) with (2.5) in a general way as

$$a \times (2.1) + b \times (2.2), \qquad c \times (2.4) + d \times (2.5) \tag{2.14}$$

where a, b, c, and d are combination factors. The resulting equations can be written as

$$\begin{bmatrix} a\mathcal{T}_1 + b\dfrac{\eta_2}{\eta_1}\mathcal{T}_2 & \dfrac{a-b}{2}\mathcal{I} - a\mathcal{K}_1 - b\mathcal{K}_2 \\ \dfrac{-c+d}{2}\mathcal{I} + c\mathcal{K}_1 + d\mathcal{K}_2 & c\mathcal{T}_1 + d\dfrac{\eta_1}{\eta_2}\mathcal{T}_2 \end{bmatrix} \begin{bmatrix} \eta_1 \boldsymbol{J} \\ \boldsymbol{M} \end{bmatrix} = \begin{bmatrix} -a\,\hat{\boldsymbol{n}} \times \boldsymbol{E}_1^{\text{inc}} + b\,\hat{\boldsymbol{n}} \times \boldsymbol{E}_2^{\text{inc}} \\ -c\,\eta_1 \hat{\boldsymbol{n}} \times \boldsymbol{H}_1^{\text{inc}} + d\,\eta_1 \hat{\boldsymbol{n}} \times \boldsymbol{H}_2^{\text{inc}} \end{bmatrix}. \tag{2.15}$$

Several well-known equations can be obtained by choosing different combination factors. For example,

1. by choosing $a = b = c = d = 1$, the PMCHWT equations [4–6] can be obtained; and

2. by choosing $a = -1$, $b = \varepsilon_r = \varepsilon_2/\varepsilon_1$, $c = 1$, $d = -\mu_r = -\mu_2/\mu_1$, the Müller equations [8, 9] can be obtained.

More explicitly, the PMCHWT equations can be expressed as

$$\begin{bmatrix} \mathcal{T}_1 + \dfrac{\eta_2}{\eta_1}\mathcal{T}_2 & -\mathcal{K}_1 - \mathcal{K}_2 \\ \mathcal{K}_1 + \mathcal{K}_2 & \mathcal{T}_1 + \dfrac{\eta_1}{\eta_2}\mathcal{T}_2 \end{bmatrix} \begin{bmatrix} \eta_1 \boldsymbol{J} \\ \boldsymbol{M} \end{bmatrix} = \begin{bmatrix} -\hat{\boldsymbol{n}} \times \boldsymbol{E}_1^{\text{inc}} + \hat{\boldsymbol{n}} \times \boldsymbol{E}_2^{\text{inc}} \\ -\eta_1 \hat{\boldsymbol{n}} \times \boldsymbol{H}_1^{\text{inc}} + \eta_1 \hat{\boldsymbol{n}} \times \boldsymbol{H}_2^{\text{inc}} \end{bmatrix} \tag{2.16}$$

and the Müller equations can be expressed as

$$\begin{aligned} &\begin{bmatrix} -\dfrac{1+\mu_r}{2}\mathcal{I} + \mathcal{K}_1 - \mu_r \mathcal{K}_2 & \mathcal{T}_1 - \dfrac{k_2}{k_1}\mathcal{T}_2 \\ -\mathcal{T}_1 + \dfrac{k_2}{k_1}\mathcal{T}_2 & -\dfrac{1+\varepsilon_r}{2}\mathcal{I} + \mathcal{K}_1 - \varepsilon_r \mathcal{K}_2 \end{bmatrix} \begin{bmatrix} \eta_1 \boldsymbol{J} \\ \boldsymbol{M} \end{bmatrix} \\ &\qquad = \begin{bmatrix} -\eta_1 \hat{\boldsymbol{n}} \times \boldsymbol{H}_1^{\text{inc}} - \eta_1 \mu_r \hat{\boldsymbol{n}} \times \boldsymbol{H}_2^{\text{inc}} \\ \hat{\boldsymbol{n}} \times \boldsymbol{E}_1^{\text{inc}} + \varepsilon_r \hat{\boldsymbol{n}} \times \boldsymbol{E}_2^{\text{inc}} \end{bmatrix}. \end{aligned} \tag{2.17}$$

Although there are other ways to formulate SIEs for the dielectric case, such as by using a different combination strategy [36, 37], or even applying different forms of the equivalence principle [38, 39], only the PMCHWT and the Müller equations are discussed in this thesis since they correspond to the Fredholm integral equations of the first and the second kind, respectively, as pointed out in [7, 20], and [10]. As a matter of fact, since in the PMCHWT equations (2.16), the identity operators are canceled out, leaving only $\mathcal{K}$ operators, which are compact operators, in the off-diagonal blocks, and $\mathcal{T}$ operators in the diagonal blocks, the resulting equations are the first-kind Fredholm integral equations. In the Müller equations (2.17), on the other hand, the hyper-singular terms of the $\mathcal{T}$ operators are canceled, resulting in the compact operators $\pm\left[\mathcal{T}_1 - (k_2/k_1)\,\mathcal{T}_2\right]$ in the off-diagonal blocks [9, 10], and the diagonal blocks are in the forms of the identity operators plus the compact $\mathcal{K}$ operators. Therefore, the Müller equations are the second-kind Fredholm integral equations. Similar to the EFIE and the MFIE in the PEC case, the PMCHWT equations are known to have a better accuracy than the Müller equations, while the latter has a faster convergence rate in an iterative solution [20].

In the following sections, the general formulations for an electromagnetic problem are simplified into two special cases, one of which is the commonly solved scattering problem, and the other one is related to the extinction theorem [30, 31], which can be used for the accurate evaluation of the numerical errors in the solution of the integral equations.

2.2 Scattering Problems

If there are only incident waves coming from the exterior region of Ω_2, the aforementioned problem is degenerated into the well-known scattering problem.

2.2.1 The PEC Case

If the object Ω_2 is a PEC, the application of the boundary condition $\hat{\boldsymbol{n}}\times\boldsymbol{E}=0$ results in $\boldsymbol{M}=0$, which, when substituted into (2.1) and (2.4), yields the EFIE and the MFIE in the PEC case as

$$\mathcal{T}_1\left(\eta_1\boldsymbol{J}\right) = -\hat{\boldsymbol{n}}\times\boldsymbol{E}_1^{\text{inc}} \tag{2.18}$$

$$-\frac{\eta_1\boldsymbol{J}}{2}+\mathcal{K}_1\left(\eta_1\boldsymbol{J}\right) = -\eta_1\hat{\boldsymbol{n}}\times\boldsymbol{H}_1^{\text{inc}}. \tag{2.19}$$

2.2.2 The Dielectric Case

If the object is a dielectric with only the exterior excitation, the PMCHWT and the Müller equations can be simplified to

$$\begin{bmatrix}\mathcal{T}_1+\dfrac{\eta_2}{\eta_1}\mathcal{T}_2 & -\mathcal{K}_1-\mathcal{K}_2\\ \mathcal{K}_1+\mathcal{K}_2 & \mathcal{T}_1+\dfrac{\eta_1}{\eta_2}\mathcal{T}_2\end{bmatrix}\begin{bmatrix}\eta_1\boldsymbol{J}\\ \boldsymbol{M}\end{bmatrix} = \begin{bmatrix}-\hat{\boldsymbol{n}}\times\boldsymbol{E}_1^{\text{inc}}\\ -\eta_1\hat{\boldsymbol{n}}\times\boldsymbol{H}_1^{\text{inc}}\end{bmatrix} \tag{2.20}$$

and

$$\begin{bmatrix}-\dfrac{1+\mu_r}{2}\mathcal{I}+\mathcal{K}_1-\mu_r\mathcal{K}_2 & \mathcal{T}_1-\dfrac{k_2}{k_1}\mathcal{T}_2\\ -\mathcal{T}_1+\dfrac{k_2}{k_1}\mathcal{T}_2 & -\dfrac{1+\varepsilon_r}{2}\mathcal{I}+\mathcal{K}_1-\varepsilon_r\mathcal{K}_2\end{bmatrix}\begin{bmatrix}\eta_1\boldsymbol{J}\\ \boldsymbol{M}\end{bmatrix} = \begin{bmatrix}-\eta_1\hat{\boldsymbol{n}}\times\boldsymbol{H}_1^{\text{inc}}\\ \hat{\boldsymbol{n}}\times\boldsymbol{E}_1^{\text{inc}}\end{bmatrix} \tag{2.21}$$

respectively.

2.2.3 Comments and Remarks

In solving an electromagnetic scattering problem, both (2.18) and (2.19) can be used to solve for $\eta_1 \boldsymbol{J}$ in the PEC case, and both (2.20) and (2.21) can be used to solve for $\eta_1 \boldsymbol{J}$ and $\boldsymbol{M}$ in the dielectric case. Once the unknown surface currents are obtained, the transverse components of the far-field responses of the object in the direction of $\hat{\boldsymbol{r}}$ can be calculated using

$$\begin{aligned} \hat{\boldsymbol{r}} \times \boldsymbol{E}_1^{\mathrm{sca}}(r \to \infty) &= \hat{\boldsymbol{r}} \times \left(\boldsymbol{E}_1^{\mathrm{tol}} - \boldsymbol{E}_1^{\mathrm{inc}}\right) \\ &= \left[\mathcal{T}_1(\eta_1 \boldsymbol{J}) - \mathcal{K}_1(\boldsymbol{M})\right]_{r\to\infty} \qquad (2.22) \\ \hat{\boldsymbol{r}} \times \eta_1 \boldsymbol{H}_1^{\mathrm{sca}}(r \to \infty) &= \hat{\boldsymbol{r}} \times \left(\eta_1 \boldsymbol{H}_1^{\mathrm{tol}} - \eta_1 \boldsymbol{H}_1^{\mathrm{inc}}\right) \\ &= \left[\mathcal{T}_1(\boldsymbol{M}) + \mathcal{K}_1(\eta_1 \boldsymbol{J})\right]_{r\to\infty} \qquad (2.23) \end{aligned}$$

and the radar cross section (RCS) in the direction of $\hat{\boldsymbol{r}}$ is defined as

$$\begin{aligned} \sigma(\hat{\boldsymbol{r}}) &= \lim_{r\to\infty} 4\pi r^2 \frac{\left|\boldsymbol{E}_1^{\mathrm{sca}}(\hat{\boldsymbol{r}})\right|^2}{\left|\boldsymbol{E}_1^{\mathrm{inc}}(\hat{\boldsymbol{r}})\right|^2} \\ &= \lim_{r\to\infty} 4\pi r^2 \frac{\left|\boldsymbol{H}_1^{\mathrm{sca}}(\hat{\boldsymbol{r}})\right|^2}{\left|\boldsymbol{H}_1^{\mathrm{inc}}(\hat{\boldsymbol{r}})\right|^2}. \qquad (2.24) \end{aligned}$$

In computational electromagnetics, the numerical error of an integral equation is often measured in terms of the relative RMS error of the RCS results, which can be expressed as

$$\mathrm{RMS}(\sigma) = \sqrt{\frac{\sum_{p=1}^{N} \left|\sigma^{\mathrm{cal}}(\hat{\boldsymbol{r}}_p) - \sigma^{\mathrm{ref}}(\hat{\boldsymbol{r}}_p)\right|^2}{\sum_{p=1}^{N} \left|\sigma^{\mathrm{ref}}(\hat{\boldsymbol{r}}_p)\right|^2}} \qquad (2.25)$$

where $\sigma^{\mathrm{cal}}(\hat{\boldsymbol{r}}_p)$ and $\sigma^{\mathrm{ref}}(\hat{\boldsymbol{r}}_p)$ stand for the calculated and the reference RCS in the direction of $\hat{\boldsymbol{r}}_p$, respectively.

After solving the integral equations (2.18)-(2.21) using Galerkin's method, and evaluating the RMS error of the RCS using (2.25), it is usually found that the first-kind integral equations (2.18) and (2.20) produce numerical results with a much better accuracy than the second-kind integral equations (2.19) and (2.21). However, in real applications, a sphere is the only three-dimensional object that has an analytical solution called the Mie series solution, which can be used as the accurate reference data in the evaluation of numerical errors. The lack of accurate reference data makes it difficult

to measure the numerical errors when solving problems for generally shaped objects. In the next section, the extinction theorem [30, 31] is applied in the other special case of the general formulations, which provides us a robust and universal approach of evaluating numerical errors for arbitrarily shaped three-dimensional objects.

2.3 Null-Field Problems

If there are only incident waves coming from the interior region of Ω_2, the electromagnetic problem is degenerated into the so-called null-field problem.

2.3.1 The PEC Case

If the object Ω_2 is a hollow PEC cavity filled with a homogeneous medium with permittivity ε_2 and permeability μ_2, the application of the boundary condition $\hat{\boldsymbol{n}} \times \boldsymbol{E} = 0$ also results in $\boldsymbol{M} = 0$, which, when substituted into (2.2) and (2.5), yields the EFIE and the MFIE in the PEC case as

$$\mathcal{T}_2\left(\eta_2 \boldsymbol{J}\right) = \hat{\boldsymbol{n}} \times \boldsymbol{E}_2^{\text{inc}} \tag{2.26}$$

$$-\frac{\eta_2 \boldsymbol{J}}{2} - \mathcal{K}_2\left(\eta_2 \boldsymbol{J}\right) = -\eta_2 \hat{\boldsymbol{n}} \times \boldsymbol{H}_2^{\text{inc}}. \tag{2.27}$$

2.3.2 The Dielectric Case

If the object is a dielectric with only the interior excitation, the PMCHWT and the Müller equations can be simplified to

$$\begin{bmatrix} \mathcal{T}_1 + \dfrac{\eta_2}{\eta_1}\mathcal{T}_2 & -\mathcal{K}_1 - \mathcal{K}_2 \\ \mathcal{K}_1 + \mathcal{K}_2 & \mathcal{T}_1 + \dfrac{\eta_1}{\eta_2}\mathcal{T}_2 \end{bmatrix} \begin{bmatrix} \eta_1 \boldsymbol{J} \\ \boldsymbol{M} \end{bmatrix} = \begin{bmatrix} \hat{\boldsymbol{n}} \times \boldsymbol{E}_2^{\text{inc}} \\ \eta_1 \hat{\boldsymbol{n}} \times \boldsymbol{H}_2^{\text{inc}} \end{bmatrix} \tag{2.28}$$

and

$$\begin{bmatrix} -\dfrac{1+\mu_r}{2}\mathcal{I} + \mathcal{K}_1 - \mu_r \mathcal{K}_2 & \mathcal{T}_1 - \dfrac{k_2}{k_1}\mathcal{T}_2 \\ -\mathcal{T}_1 + \dfrac{k_2}{k_1}\mathcal{T}_2 & -\dfrac{1+\varepsilon_r}{2}\mathcal{I} + \mathcal{K}_1 - \varepsilon_r \mathcal{K}_2 \end{bmatrix} \begin{bmatrix} \eta_1 \boldsymbol{J} \\ \boldsymbol{M} \end{bmatrix}$$

$$= \begin{bmatrix} -\eta_1 \mu_r \hat{\boldsymbol{n}} \times \boldsymbol{H}_2^{\text{inc}} \\ \varepsilon_r \hat{\boldsymbol{n}} \times \boldsymbol{E}_2^{\text{inc}} \end{bmatrix} \tag{2.29}$$

respectively.

2.3.3 Comments and Remarks

In solving an electromagnetic null-field problem, both (2.26) and (2.27) can be used to solve for $\eta_2 \boldsymbol{J}$ in the PEC case, and both (2.28) and (2.29) can be used to solve for $\eta_2 \boldsymbol{J}$ and $\boldsymbol{M}$ in the dielectric case. Once the unknown surface currents are obtained, the transverse components of the far fields radiated by the equivalent sources in the direction of $\hat{\boldsymbol{r}}$ can be calculated using

$$\hat{\boldsymbol{r}} \times \boldsymbol{E}_2^{\text{rad}} (r \to \infty) = \left[\mathcal{T}_2 (\eta_2 \boldsymbol{J}) - \mathcal{K}_2 (\boldsymbol{M}) \right]_{r \to \infty} \tag{2.30}$$

$$\hat{\boldsymbol{r}} \times \eta_2 \boldsymbol{H}_2^{\text{rad}} (r \to \infty) = \left[\mathcal{T}_2 (\boldsymbol{M}) + \mathcal{K}_2 (\eta_2 \boldsymbol{J}) \right]_{r \to \infty} . \tag{2.31}$$

According to the interior equivalent problem [30, 31], in which the exterior region Ω_1 is filled with the same homogeneous medium as what is inside Ω_2, the object Ω_2 can be removed, and its contribution can be replaced by the equivalent currents $\eta_2 \boldsymbol{J}$ and $\boldsymbol{M}$. The total fields outside Ω_2 should vanish

$$\boldsymbol{E}_2^{\text{tol}} (\boldsymbol{r}) = \boldsymbol{E}_2^{\text{inc}} (\boldsymbol{r}) + \boldsymbol{E}_2^{\text{rad}} (\boldsymbol{r}) = 0 \tag{2.32}$$

$$\eta_2 \boldsymbol{H}_2^{\text{tol}} (\boldsymbol{r}) = \eta_2 \boldsymbol{H}_2^{\text{inc}} (\boldsymbol{r}) + \eta_2 \boldsymbol{H}_2^{\text{rad}} (\boldsymbol{r}) = 0 \tag{2.33}$$

which is known as the extinction theorem. It should be noted that (2.32) and (2.33) are always true regardless of the shape of the object. This unique property makes it an excellent measure to evaluate the numerical errors in the solution of the integral equations. To be specific, define the magnitude of the transverse components of the total electric field normalized by that of the incident electric field at infinity as the numerical error due to the numerical solution of the integral equations

$$\delta (\hat{\boldsymbol{r}}) = \lim_{r \to \infty} \frac{\left| \hat{\boldsymbol{r}} \times \boldsymbol{E}_2^{\text{tol}} (\boldsymbol{r}) \right|}{\left| \hat{\boldsymbol{r}} \times \boldsymbol{E}_2^{\text{inc}} (\boldsymbol{r}) \right|} \tag{2.34}$$

the RMS error can then be defined as

$$\mathrm{RMS} = \sqrt{\frac{1}{N}\sum_{p=1}^{N} \delta^2\left(\hat{\boldsymbol{r}}_p\right)}. \tag{2.35}$$

Apparently, (2.35) is a good and universal measurement of the numerical errors in the solution of the integral equations (2.26)-(2.29) for arbitrarily shaped objects in both the PEC and the dielectric cases.

More importantly, in the PEC case, if the medium inside Ω_2 in the null-field problem is the same as the medium outside Ω_2 in the scattering problem, i.e., $\varepsilon_2 = \varepsilon_1$, and $\mu_2 = \mu_1$, the left-hand side (LHS) of the EFIE (2.26) becomes exactly the same as the LHS of the EFIE (2.18), and the LHS of the MFIE (2.27) also becomes the same as the LHS of the MFIE (2.19) with only a sign difference before the $\mathcal{K}$ operator, which is caused by the definition of the unit normal vector $\hat{\boldsymbol{n}}$. Moreover, in the dielectric case, the LHS of the PMCHWT equations (2.28) in the null-field problem is the same as that of the PMCHWT equations (2.20) in the scattering problem, and the LHS of the Müller equations (2.29) in the null-field problem is the same as that of the Müller equations (2.21) in the scattering problem. The only difference between the equations in the null-field problem and those in the scattering problem is the right-hand sides which are related to the incident fields. Therefore, the numerical error measured by (2.35) in solving a null-field problem is a good indicator of the numerical error produced by solving an integral equation in a corresponding scattering problem.

CHAPTER 3

ACCURACY IMPROVEMENT OF THE SECOND-KIND INTEGRAL EQUATIONS FOR SMOOTH OBJECTS

In this chapter, the discretization schemes for different integral operators are discussed. The discretization error due to the identity operator is then suppressed by using the rotated BC functions defined on curvilinear triangular patches [28] as the testing function. It is demonstrated through several numerical examples that the accuracy of the second-kind Fredholm integral equations (the MFIE and Müller equations), in both PEC and dielectric cases, can be improved significantly using this discretization scheme.

3.1 Discretization of Operators

All the preceding statements on the solution accuracy and iterative convergence rate are based on a certain discretization scheme, which will be described and discussed in this section. The discretization process of an integral equation mainly contains two major steps. The first step is to expand the unknown current density in terms of basis functions, and the second step is to convert the integral equation into a matrix equation through a set of testing functions. Generally speaking, the basis and testing functions can be categorized into two different kinds: the divergence-conforming and the curl-conforming functions. A typical divergence-conforming function is the curvilinear Rao-Wilton-Glisson (CRWG) function [40,41], denoted as $\boldsymbol{f}^r$. By rotating it with respect to the normal direction, a commonly used curl-conforming function $\hat{\boldsymbol{n}} \times \boldsymbol{f}^r$ can be obtained. The CRWG function has a normal component across the shared edge of two adjacent triangles, whereas the rotated CRWG function has a tangential component along the shared edge, as shown in Figures 3.1a and 3.1b, respectively. Recently, another divergence-conforming function called the Buffa-Christiansen (BC) function has been proposed [25] and successfully adopted in the implementation of the

Calderón preconditioning technique [42, 43]. As a linear combination of the CRWG functions defined on a barycentric refinement of the original triangular mesh, the BC function, denoted as $\boldsymbol{f}^b$, is strictly divergence-conforming on the barycentric mesh. At the same time, since its main component resembles that of the $\hat{\boldsymbol{n}} \times \boldsymbol{f}^r$ function, the BC function is also quasi-curl-conforming on the original mesh. By rotating $\boldsymbol{f}^b$ with respect to the normal direction, the $\hat{\boldsymbol{n}} \times \boldsymbol{f}^b$ is curl-conforming on the barycentric mesh and quasi-divergence-conforming on the original mesh. Figures 3.1c and 3.1d illustrate the definition domains and the main components of a typical BC and rotated BC functions, respectively.

Next, we discuss the discretization scheme that can be adopted to discretize the $\mathcal{T}$, $\mathcal{I}$, and $\mathcal{K}$ operators, respectively. To this end, the unknown current density $\boldsymbol{X}$ is first expanded in terms of a set of basis functions, and the integral operator is then tested by a set of testing functions. It is a physical requirement that the basis function should be divergence-conforming in order to model the current (field) continuity correctly and to give a good representation of the $\nabla \cdot \boldsymbol{X}$ term which is related to the surface (electric/magnetic) charge density. Because of its popularity and simplicity in definition, the CRWG function $\boldsymbol{f}^r$ is employed as the basis function throughout this chapter.

$$\boldsymbol{X} = \sum_{n=1}^{N} a_n \boldsymbol{f}_n^r \tag{3.1}$$

where N is the number of interior edges in a triangular mesh of the object, and a_n are the expansion coefficients to be determined.

Table 3.1: Comparison of Different Testing Functions in the Discretization of the $\mathcal{T}$ Operator ($\boldsymbol{f}_n^r$ as the Basis Function)

	Math Property	Well-Tested	Contour Int.
$\boldsymbol{f}_m^r$	Div.-Conf.	No	Yes
$\hat{\boldsymbol{n}} \times \boldsymbol{f}_m^r$	Cur.-Conf.	Yes	No
$\boldsymbol{f}_m^b$	Div.-Conf.	Yes	Yes
$\hat{\boldsymbol{n}} \times \boldsymbol{f}_m^b$	Cur.-Conf.	No	No

3.1.1 The $\mathcal{T}$ Operator

Since the testing procedure is nothing but a mathematical manipulation, in principle, both divergence- and curl-conforming testing functions can be used. However, there are some mathematical issues need to be noted. First, in order to have the $\mathcal{T}$ operator well-tested, the testing function should be orthogonal to the basis function. From this point of view, the good testing functions are $\hat{\boldsymbol{n}} \times \boldsymbol{f}^r$ and $\boldsymbol{f}^b$. Second, the use of the divergence-conforming testing function will lead to a contour integration in the discretization of the $\mathcal{T}$ operator, which is not easy to be evaluated accurately and hence it is undesired. Denoting $\boldsymbol{t}_m$ as the testing function, the discretization of the $\mathcal{T}$ operator yields

$$\begin{aligned} Z_{mn}^{\mathcal{T}} =& ik_j \int_{S_m} \boldsymbol{t}_m \cdot \hat{\boldsymbol{n}} \times \int_{S_n} \left(\mathcal{I} + \frac{\nabla\nabla}{k_j^2} \right) G(\boldsymbol{r}, \boldsymbol{r}'; k_j) \cdot \boldsymbol{f}_n^r \mathrm{d}\boldsymbol{r}' \mathrm{d}\boldsymbol{r} \\ =& ik_j \int_{S_m} \int_{S_n} \boldsymbol{t}_m \times \hat{\boldsymbol{n}} \cdot \boldsymbol{f}_n^r G \\ & + \frac{1}{k_j^2} [\nabla \cdot (\boldsymbol{t}_m \times \hat{\boldsymbol{n}} G) - G \nabla \cdot (\boldsymbol{t}_m \times \hat{\boldsymbol{n}})] \nabla' \cdot \boldsymbol{f}_n^r \mathrm{d}\boldsymbol{r}' \mathrm{d}\boldsymbol{r}. \end{aligned} \tag{3.2}$$

If $\boldsymbol{t}_m$ is divergence-conforming, for example, $\boldsymbol{t}_m = \boldsymbol{f}_m^r$ or $\boldsymbol{f}_m^b$, the surface integration of $\nabla \cdot \left(\boldsymbol{f}_m^{r,b} \times \hat{\boldsymbol{n}}\ G \right)$ becomes a contour integral, and furthermore, $\nabla \cdot \left(\boldsymbol{f}_m^{r,b} \times \hat{\boldsymbol{n}} \right)$ vanishes within each triangle that supports $\boldsymbol{f}_m^{r,b}$, yielding

$$\begin{aligned} Z_{mn}^{\mathcal{T}} =& ik_j \int_{S_m} \int_{S_n} \boldsymbol{f}_m^{r,b} \times \hat{\boldsymbol{n}} \cdot \boldsymbol{f}_n^r G \mathrm{d}\boldsymbol{r}' \mathrm{d}\boldsymbol{r} \\ & + \frac{i}{k_j} \oint_{C_m} \int_{S_n} \hat{\boldsymbol{l}} \cdot \boldsymbol{f}_m^{r,b} \times \hat{\boldsymbol{n}}\ G\ \nabla' \cdot \boldsymbol{f}_n^r \mathrm{d}\boldsymbol{r}' \mathrm{d}\boldsymbol{r} \end{aligned} \tag{3.3}$$

where $\hat{\boldsymbol{l}}$ is the outward-pointing unit normal vector defined on the integral boundary C_m which comprises the boundaries of the triangles that support $\boldsymbol{f}_m^{r,b}$. If $\boldsymbol{t}_m$ is curl-conforming, $\boldsymbol{t}_m = \hat{\boldsymbol{n}} \times \boldsymbol{f}_m^r$ or $\hat{\boldsymbol{n}} \times \boldsymbol{f}_m^b$, the surface integration of $\nabla \cdot \left(\hat{\boldsymbol{n}} \times \boldsymbol{f}_m^{r,b} \times \hat{\boldsymbol{n}}\ G \right) = \nabla \cdot \left(\boldsymbol{f}_m^{r,b}\ G \right)$ vanishes as a result of the Gauss divergence theorem, yielding

$$Z_{mn}^{\mathcal{T}} = ik_j \int_{S_m} \int_{S_n} \left(\boldsymbol{f}_m^{r,b} \cdot \boldsymbol{f}_n^r - \frac{1}{k_j^2} \nabla \cdot \boldsymbol{f}_m^{r,b} \nabla' \cdot \boldsymbol{f}_n^r \right) G \mathrm{d}\boldsymbol{r}' \mathrm{d}\boldsymbol{r}. \tag{3.4}$$

Obviously, (3.4) is easier to implement than (3.3) since it avoids the evaluation of the contour integral. Shown in Table 3.1 is the comparison of different testing functions used in the discretization of the $\mathcal{T}$ operator. From this table, it is clear that the $\hat{\boldsymbol{n}} \times \boldsymbol{f}_m^r$ function is the best candidate for a testing function, since it will result in a well-tested $\mathcal{T}$ operator and a simple mathematical expression of the integral which can be evaluated accurately.

3.1.2 The $\mathcal{I}$ Operator

At the first glance, the identity operator $\mathcal{I}$ is usually considered the simplest operator in terms of discretization. In the testing procedure, the identity operator is well-tested as long as the testing function lies in the same direction as that of the basis function. From this point of view, the good testing functions are $\boldsymbol{f}_m^r$ and $\hat{\boldsymbol{n}} \times \boldsymbol{f}_m^b$, while the first one is commonly used.

If the discretization of the $\mathcal{I}$ operator is considered from a different perspective, it can be found out that, although the discretization of the identity operator may have an analytical expression which allows the evaluation of the integration to be exact, the integral kernel is actually highly singular. Since the discretization of the $\mathcal{I}$ operator can be expressed as [22]

$$\begin{aligned} Z_{mn}^{\mathcal{I}} &= \int_{S_m} \boldsymbol{t}_m(\boldsymbol{r}) \cdot \mathcal{I}\big[\, \boldsymbol{f}_n^r(\boldsymbol{r}) \,\big] \, \mathrm{d}\boldsymbol{r} \\ &= \int_{S_m} \boldsymbol{t}_m(\boldsymbol{r}) \cdot \int_{S_n} \delta(\boldsymbol{r}, \boldsymbol{r}') \; \boldsymbol{f}_n^r(\boldsymbol{r}') \; \mathrm{d}\boldsymbol{r}' \mathrm{d}\boldsymbol{r} \end{aligned} \tag{3.5}$$

the implied integral kernel $\delta(\boldsymbol{r}, \boldsymbol{r}')$ is highly singular at $\boldsymbol{r} = \boldsymbol{r}'$. It finally turns out that it is the discretization of the identity operator that contributes significantly to the total error of the second-kind integral equations [22]. Although the regularization methods [23, 24] can be employed to reduce this discretization error, they are not widely used because of the reason mentioned in Chapter 1. In this chapter, it is shown that the discretization error due to the identity operator can be reduced greatly by choosing the $\hat{\boldsymbol{n}} \times \boldsymbol{f}_m^b$ function instead of the $\boldsymbol{f}_m^r$ function as the testing function. It is also demonstrated that, by using this discretization scheme, the accuracy of the second-kind Fredholm integral equations can be improved significantly.

3.1.3 The $\mathcal{K}$ Operator

Since in most cases the $\mathcal{K}$ operator comes along with the $\mathcal{I}$ operator, the choice of the testing function should be the same as that of the $\mathcal{I}$ operator, which was discussed earlier. Nevertheless, it should be pointed out that, whatever function is chosen as the testing function, as long as the basis and testing functions lie in the same plane in a specific geometric discretization of the object, the impedance element given by

$$\begin{aligned} Z_{mn}^{\mathcal{K}} &= \int_{S_m} P.V. \int_{S_n} \boldsymbol{t}_m \cdot \hat{\boldsymbol{n}} \times \nabla G(\boldsymbol{r}, \boldsymbol{r}'; k_j) \times \boldsymbol{f}_n^r \mathrm{d}\boldsymbol{r}' \mathrm{d}\boldsymbol{r} \\ &= \int_{S_m} P.V. \int_{S_n} \left(ik_j - \frac{1}{R} \right) \frac{G}{R} \left(\hat{\boldsymbol{n}} \times \boldsymbol{t}_m \right) \cdot \left(\boldsymbol{f}_n^r \times \boldsymbol{R} \right) \mathrm{d}\boldsymbol{r}' \mathrm{d}\boldsymbol{r} \end{aligned} \tag{3.6}$$

is always zero, because the magnetic (electric) field (at the point $\boldsymbol{r}$) produced by the electric (magnetic) current (at the point $\boldsymbol{r}'$) is perpendicular to the plane formed by the current vector $\boldsymbol{f}_n^r$ and the vector $\boldsymbol{R} = \boldsymbol{r} - \boldsymbol{r}'$. Clearly, as long as the surface of the object is smooth, the near-field interaction, where $R = |\boldsymbol{R}|$ is small, is always very weak, because the singularity in the integral kernel has been excluded from (3.6). This can be regarded as an algebraic interpretation of the concept "compact operator". Consequently, it is also very clear that the $\mathcal{K}$ operator is no longer a compact operator if the surface of the object is not smooth, for example, if there are corners or sharp tips on the object.

3.2 Discretization of SIEs

Based on the investigations above, adequate discretization schemes can be adopted to transform the SIEs into matrix equations. Both the conventional scheme and the scheme presented in this chapter will be discussed.

3.2.1 SIEs of the First Kind

According to Table 3.1, $\hat{\boldsymbol{n}} \times \boldsymbol{f}_m^r$ is the most suitable testing function to discretize the EFIE (2.18). For the PMCHWT equations (2.20), as long as the diagonal $\mathcal{T}$ operators are well tested, the whole equations can be solved

accurately. Therefore, the $\hat{\boldsymbol{n}} \times \boldsymbol{f}_m^r$ function is also a good testing function to discretize the PMCHWT equations.

3.2.2 SIEs of the Second Kind

Since the different choices of the testing functions will not change the compactness of the $\mathcal{K}$ operator, it is sufficient to have a good discretization of the MFIE (2.19) as long as the $\mathcal{I}$ operator is well tested. Based on the discussion earlier, both $\boldsymbol{f}_m^r$ and $\hat{\boldsymbol{n}} \times \boldsymbol{f}_m^b$ are the adequate testing functions to discretize the MFIE. However, as will be shown in the following sections, the use of the $\boldsymbol{f}_m^r$ testing function, which is a conventional way to discretize the MFIE, will produce a much larger error compared to the choice of the $\hat{\boldsymbol{n}} \times \boldsymbol{f}_m^b$ as the testing function. Hence, the latter is recommended for the discretization of the MFIE, as proposed in [26]. It is also necessary to point out that, for the discretization of the CFIE (2.13), $\boldsymbol{f}_m^r$ is also a good testing function since the $\mathcal{T}$ operator is rotated by $\hat{\boldsymbol{n}}$, which corresponds to the conventional way of discretizing the CFIE. However, if the $\hat{\boldsymbol{n}} \times \boldsymbol{f}_m^b$ testing function is applied directly to (2.13), although both the EFIE and the MFIE parts are adequately discretized and well tested, there will be a contour integral in the EFIE part (see Table 3.1). Since the contour of the BC function is very complex, there is no way to achieve both high accuracy and efficiency in the evaluation of this integral at the same time. In this chapter, a mixed discretization scheme is adopted for the discretization of the CFIE, which uses the $\hat{\boldsymbol{n}} \times \boldsymbol{f}_m^r$ testing function to discretize the EFIE (2.18) and the $\hat{\boldsymbol{n}} \times \boldsymbol{f}_m^b$ testing function to discretize the MFIE (2.19) before summing them up.

Similarly, since the off-diagonal blocks are compact, it is sufficient to have a good discretization of the Müller equations (2.21) as long as the diagonal blocks are well tested. Similar to the MFIE in the PEC case, both $\boldsymbol{f}_m^r$ and $\hat{\boldsymbol{n}} \times \boldsymbol{f}_m^b$ are the adequate testing functions. In fact, the $\boldsymbol{f}_m^r$ testing function has been commonly used [9], which resulted in a contour integration in the evaluation of the $\mathcal{T}$ operators. In contrast, the use of the $\hat{\boldsymbol{n}} \times \boldsymbol{f}_m^b$ testing function can not only have a well-tested diagonal blocks, but also avoid the appearance of the undesired contour integral. More importantly, the use of the $\hat{\boldsymbol{n}} \times \boldsymbol{f}_m^b$ testing function will significantly suppress the discretization error of the identity operators, and hence improve the accuracy of the Müller

equations, as will be demonstrated in the next section.

3.3 Accuracy Improvement of the Identity Operator

In this section, the accuracy improved by the use of the rotated BC function as the testing function is investigated through a well-defined numerical test. Consider a plane wave ($\boldsymbol{E}^{\text{inc}}$, $\boldsymbol{H}^{\text{inc}}$) traveling in the free space. By defining a closed mathematical surface with an arbitrary shape, a set of non-radiating equivalent surface current can be found through the relation [22]

$$\begin{bmatrix} \eta_1 \boldsymbol{J}^{\text{inc}} \\ \boldsymbol{M}^{\text{inc}} \end{bmatrix} = \begin{bmatrix} \mathcal{I} & \\ & \mathcal{I} \end{bmatrix} \begin{bmatrix} \eta_1 \boldsymbol{J}^{\text{inc}} \\ \boldsymbol{M}^{\text{inc}} \end{bmatrix} = \begin{bmatrix} \eta_1 \hat{\boldsymbol{n}} \times \boldsymbol{H}^{\text{inc}} \\ -\hat{\boldsymbol{n}} \times \boldsymbol{E}^{\text{inc}} \end{bmatrix}. \tag{3.7}$$

Expanding the equivalent currents with two sets of CRWG basis functions $\boldsymbol{f}_n^r$, and testing the two equations with two sets of testing functions $\boldsymbol{t}_m$, (3.7) can be transformed into a matrix equation, which can be solved for the expansion coefficients of the basis functions. Since ($\eta_1 \boldsymbol{J}^{\text{inc}}$, $\boldsymbol{M}^{\text{inc}}$) should not radiate, their transverse radiated electric field in the far zone

$$\hat{\boldsymbol{n}} \times \boldsymbol{E}^{\text{rad}} = \mathcal{T}_1 \left(\eta_1 \boldsymbol{J}^{\text{inc}} \right) - \frac{\boldsymbol{M}^{\text{inc}}}{2} - \mathcal{K}_1 \left(\boldsymbol{M}^{\text{inc}} \right) \tag{3.8}$$

where $\hat{\boldsymbol{n}} = \hat{\boldsymbol{r}}$, can be regarded as the numerical error due to the discretization of the identity operators in (3.7). Following the definition in [22], we define the far-zone electric field as

$$E_{\infty}^{\text{rad}} \left(\boldsymbol{r}_p \right) = \lim_{r \to \infty} \left\{ r \sqrt{\left| E_{\theta}^{\text{rad}} \left(\boldsymbol{r}_p \right) \right|^2 + \left| E_{\phi}^{\text{rad}} \left(\boldsymbol{r}_p \right) \right|^2} \right\} \tag{3.9}$$

where E_{θ}^{rad} and E_{ϕ}^{rad} stand for the θ and ϕ components of the radiated electric field $\boldsymbol{E}^{\text{rad}}$, the sampling points $\boldsymbol{r}_p = (r, \theta, \phi_p)$ are on the x-y plane with $\theta = \pi/2$ and $\phi_p = (p-1)\,\pi/360$ for $p = 1, 2, \cdots, 720$. Then, the root mean square (RMS) of the radiated field, which is also the RMS error due to the discretization of the identity operators, can be calculated as

$$\text{RMS} \left\{ E_{\infty}^{\text{rad}} \right\} = \sqrt{\frac{1}{720} \sum_{p=1}^{720} \left\{ E_{\infty}^{\text{rad}} \left(\boldsymbol{r}_p \right) \right\}^2}. \tag{3.10}$$

As the numerical test, a 50-MHz plane wave is incident on a closed mathematical surface with a shape of a sphere and a cube, respectively. The radius of the sphere is 1.0 m and the size of the cube is $1.0 \times 1.0 \times 1.0$ m^3. Shown in Figures 3.2a and 3.2b are the RMS error in the calculation of the far field defined by (3.10) as a function of the discretization density for the sphere and the cube, respectively. The same test is repeated at 1.0 GHz and the results are shown in Figures 3.3a and 3.3b. In all these figures, both the CRWG functions $\boldsymbol{f}_m^r$ and the rotated BC functions $\hat{\boldsymbol{n}} \times \boldsymbol{f}_m^b$ are chosen as the testing functions $\boldsymbol{t}_m$ for the discretization of the identity operators. It is very evident that by choosing the rotated BC function as the testing function, the discretization error of the identity operator can be suppressed significantly, which serves as the major reason for the accuracy improvement of the second-kind SIEs, as will be shown in the next section.

3.4 Accuracy Improvement of the Surface Integral Equations

In this section, the accuracy of the first- and the second-kind Fredholm integral equations in both PEC and dielectric cases will be compared, using the discretization schemes discussed in Section 3.2. Although it is understood that other factors mentioned in Chapter 1, such as the inaccurate evaluation of the $\mathcal{K}$ operator, also contribute to the error of the second-kind SIEs, only the error due to the discretization of the identity operators is investigated in this chapter. Therefore, no special treatments such as those described in [11–19] are adopted here. The numerical model used is a sphere with a radius of 1.0 m, which has an analytical Mie-series solution that can be used as the reference data for comparison.

3.4.1 The PEC Case

The first- and the second-kind Fredholm integral equations in the PEC case are the EFIE (2.18) and the MFIE (2.19), respectively. Shown in Figures 3.4a and 3.4b are the RMS error in the radar cross section (RCS) of a PEC sphere calculated by the EFIE and the MFIE under the excitation of a 75-MHz and a 150-MHz plane wave, respectively. In these two figures, the accuracy of

the EFIE and those of the MFIE with two different testing schemes are compared, with respect to the discretization density. Evidently, by using the CRWG function as the testing function, the MFIE gives a larger error than the EFIE, as has been commonly observed. However, when the rotated BC function is employed as the testing function, the MFIE gives a much smaller error, even smaller than that of the EFIE, thanks to the error suppression in the discretization of the identity operator.

By setting the combination factor in the CFIE (2.13) to be $\alpha = 0.5$, its accuracy is also investigated by using the CRWG testing scheme and the mixed testing scheme described in the preceding section. From Figures 3.5a and 3.5b, it is obvious that the accuracy of the CFIE by using the CRWG testing scheme is between those of the EFIE and the MFIE using the same testing scheme, and the accuracy of the CFIE by using the mixed testing scheme is between those of the EFIE and the MFIE using the rotated BC function as the testing function, as expected.

Since the MFIE under the mixed discretization scheme has both better accuracy and faster iterative convergence than the EFIE, it is always desired to set the combination factor in the CFIE (2.13) as small as possible, as long as the existence of the EFIE part is sufficient to eliminate the spurious interior resonance. This is in contrast to the traditional CFIE, in which a compromise has to be made on the choice of the combination factor since a large value yields a slowly convergent but accurate solution, whereas a small value yields a fast convergent but inaccurate solution. This is investigated in Figures 3.6 and 3.7. In Figures 3.6a and 3.6b, the accuracy and convergence of the CFIE with two different discretization schemes are investigated at 75 MHz, which is far from the interior resonance. The RMS error of the RCS and the iteration counts needed by the BiCGstab(1) [44,45] iterative solution to achieve a relative residual error (RSS) of 10^{-6} are shown as functions of the combination factor α, where $\alpha = 0$ corresponds to the MFIE and $\alpha = 1$ corresponds to the EFIE. From Figure 3.6a, it can be seen that the smallest RMS error of the CFIE with the CRWG testing scheme can be achieved at $\alpha = 1$ at the expense of a larger iteration number, while the smallest iteration count can be achieved at $\alpha = 0$ at the cost of a larger error. Therefore, a compromise has to be made between the accuracy and efficiency. From Figure 3.6b, in contrast, both the smallest RMS error and iteration count are achieved at $\alpha = 0$, which corresponds to the MFIE with

the rotated-BC testing scheme. To demonstrate the necessity of the EFIE, the same comparison is made at the first resonant frequency of the 1.0-m spherical cavity filled with air. Theoretically, the first resonant frequency of the unit spherical cavity is 131.016 MHz. However, due to the numerical discretization process, there is a small shift on the actual numerical resonant frequency. In this chapter, the numerical resonant frequency is found to locate at 131.005 MHz by frequency searching using the MFIE with the rotated-BC testing scheme. Figures 3.7a and 3.7b show the comparison of the CFIE with two different discretization schemes at this resonant frequency. It can be seen from both figures that by introducing a small combination factor, the numerical error of the MFIE due to the interior resonance can be effectively suppressed. From Figure 3.7a, it is clear that with CRWG used as the testing function, the optimal combination factor for the RMS error is $\alpha = 1.0$, while the optimal choice to achieve the smallest iteration count is around $\alpha = 0.15$. Hence a compromise is needed. However, from Figure 3.7b, it is seen that with the mixed testing scheme, the optimal combination factor for both the RMS error and the iteration count is around $\alpha = 0.2 \sim 0.3$. The following observations can also be made from Figures 3.6 and 3.7.

1. The accuracy of the CFIE with the mixed discretization scheme is better than that with the CRWG discretization scheme in the entire range of α.

2. The convergence of the CFIE with the mixed discretization scheme is almost the same as that with the CRWG discretization scheme.

3.4.2 The Dielectric Case

The first- and the second-kind Fredholm integral equations in the dielectric case are the PMCHWT equations (2.20) and the Müller equations (2.21), respectively. Shown in Figures 3.8a and 3.8b are the RMS error in the RCS of a dielectric sphere calculated by (2.20) and (2.21), versus the discretization density. In Figure 3.8a, a 75-MHz plane wave is incident on the sphere with a radius of 1.0 m and the dielectric parameter $\varepsilon_r = 2.6$ and $\mu_r = 1.0$. In Figure 3.8b, a 100-MHz plane wave is incident on the sphere with the dielectric parameter $\varepsilon_r = 4.0$ and $\mu_r = 1.0$. From these two figures, similar observations to those in the PEC case can be made. By using the CRWG

testing scheme, the Müller equations give a larger error than the PMCHWT equations, as has been commonly observed. When the proposed rotated-BC testing scheme is employed, the Müller equations give a smaller error than the PMCHWT equations. The main reasons of the accuracy improvement of the Müller equations are as follows.

1. The use of the rotated BC testing functions suppresses the discretization error of the identity operators significantly.

2. The use of the rotated BC testing functions avoids the contour integral in $\mathcal{T}$ operators, hence resulting in a more accurate and efficient evaluation of the impedance elements from the discretization of the $\mathcal{T}$ operators.

Figures 3.9a and 3.9b show the iteration counts required by the PMCHWT and the Müller equations in a BiCGstab(1) iterative solution in order to achieve a RSS of 10^{-6}. Apparently, the convergence rates of the second-kind SIEs using CRWG testing scheme and rotated-BC testing scheme are almost the same, due to the obvious reason that both schemes test the identity operators well and maintain the compactness of the remainder parts, which yield the matrix equations with condition numbers that are not only small, but also invariant with respect to the discretization density. On the other hand, the iteration counts needed by the first-kind SIEs increase exponentially with the increase of the discretization density, similar to that observed in the EFIE for the PEC case.

An example is next designed to test the performances of the first- and the second-kind integral equations for the dielectric case at an interior resonant frequency of an object, which is a dielectric sphere with a radius of 1.0 m and the relative permittivity and permeability of $\varepsilon_r = 4.0$ and $\mu_r = 1.0$, respectively. The lowest analytical resonant frequency of the corresponding spherical cavity filled with air is 131.016 MHz. Frequency search has been applied using the EFIE (2.3) for the dielectric case to locate the numerical resonant frequency, which is 131.036 MHz under a specific curvilinear triangular discretization. Figure 3.10a shows the condition numbers of the impedance matrices obtained by discretizing the EFIE, the PMCHWT, the Müller with the RWG testing scheme, and the Müller with the rotated-BC testing scheme, as a function of the frequency in a small band around the

analytical resonant frequency. A very small frequency step, which is 1.0 kHz, is used around 131.016 MHz in the frequency search in order to obtain a smooth curve for the condition number and the correct numerical resonant frequency. It can be seen that the rotated-BC testing scheme dose not deteriorate the immunity of the interior resonance corruption of the Müller equations. The convergence histories of the four different formulations at the numerical resonant frequency are given in Figure 3.10b. It is clear that the Müller equations with both testing schemes can converge to the desired RSS of 10^{-6} much more rapidly than their first-kind counterpart which is the PMCHWT equations, while the EFIE for the dielectric case has a very slow convergence due to the interior resonance corruption.

3.5 Summary

In this chapter, the mathematical characteristics of the operators involved in the integral equations are discussed and the corresponding discretization strategies are studied. The rotated BC function is shown, both theoretically and numerically, to be a better testing function for the discretization of the second-kind integral equations for both the PEC and the dielectric cases. It is demonstrated through some numerical experiments that by using the presented discretization scheme, the discretization error of the identity operator, which is shown to be a major error source of the second-kind integral equations, can be suppressed significantly. As a result, the overall numerical error of the second-kind surface integral equations in both the PEC and the dielectric cases can be reduced significantly, leading to accurate numerical solutions that are comparable to (or even better than) the existing solutions of their first-kind counterparts in the solutions of scattering from smooth objects. At the same time, the fast convergence of the second-kind integral equations are maintained with the rotated-BC testing scheme. In the PEC case, the CFIE with a mixed discretization scheme is proposed to eliminate the spurious interior resonance corruption, and the optimal choice of the combination factor is shown to be around 0.2 to 0.3. In the dielectric case, the proposed rotated-BC testing scheme maintains the immunity of the spurious interior resonance corruption of the Müller equations, leading to an accurate and fast convergent formulation at all frequencies.

3.6 Figures

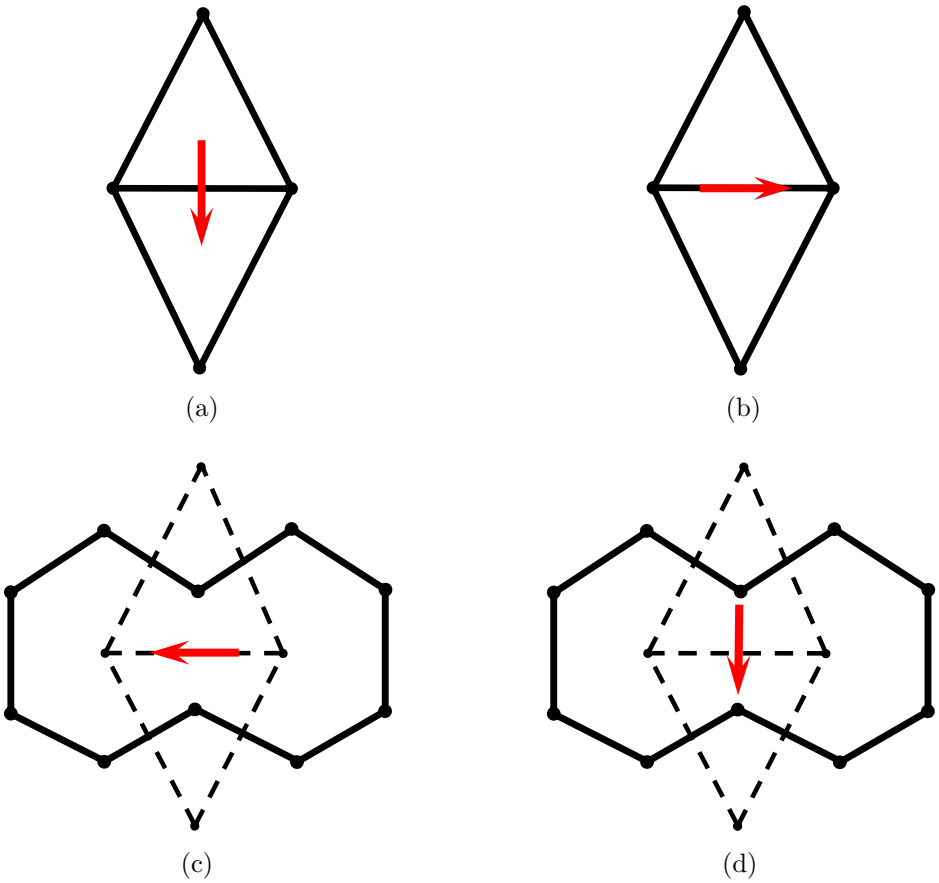

Figure 3.1: The sketches of the four functions. (a) The RWG function. (b) The rotated RWG function ($\hat{\boldsymbol{n}}\times$RWG). (c) The BC function. (d) The rotated BC function ($\hat{\boldsymbol{n}}\times$BC).

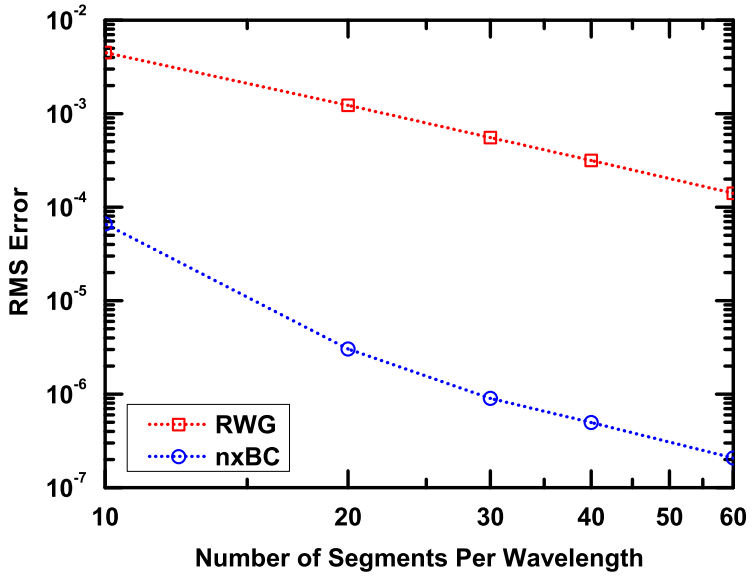

(a)

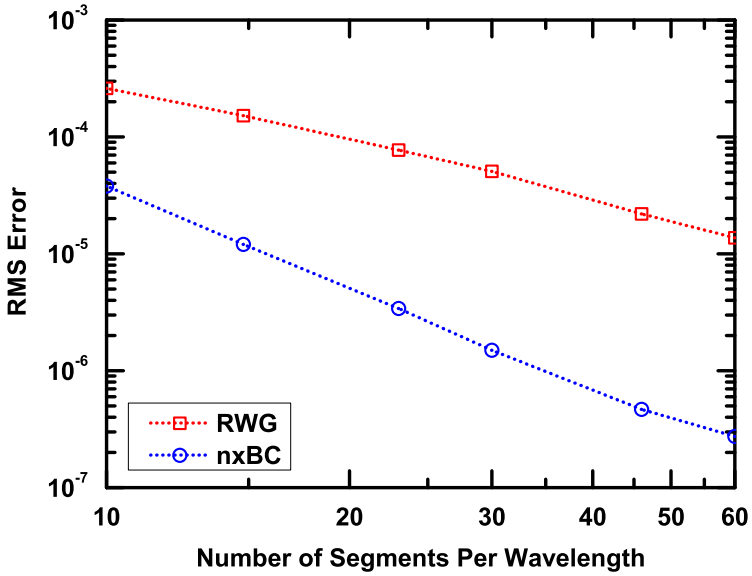

(b)

Figure 3.2: RMS of the far field as a function of the discretization density of the closed surface. The frequency of the incident plane wave is 50 MHz. Both the CRWG and the rotated BC functions are chosen as the testing functions in the discretization of the identity operators. (a) A sphere with a radius of 1.0 m. (b) A cube with a size of $1.0 \times 1.0 \times 1.0$ m^3.

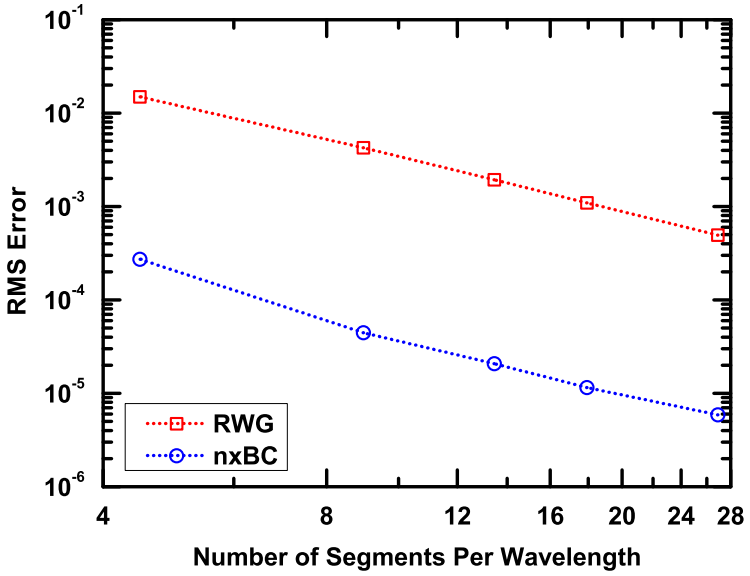

(a)

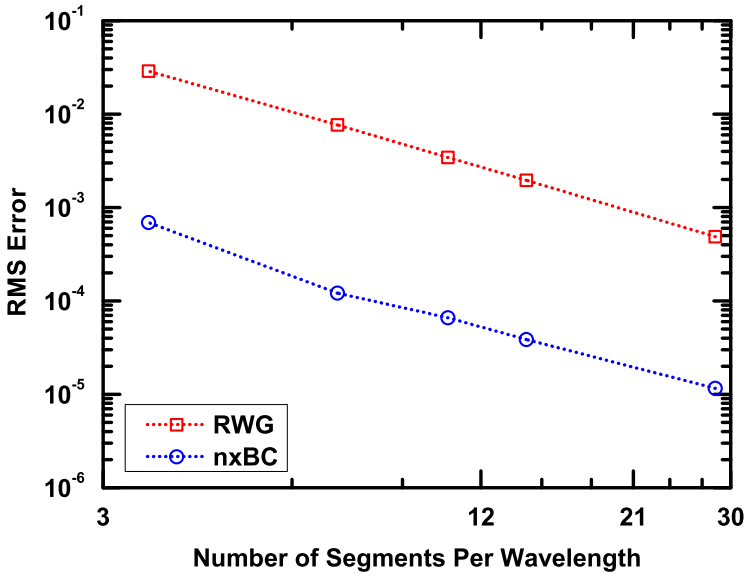

(b)

Figure 3.3: RMS of the far field as a function of the discretization density of the closed surface. The frequency of the incident plane wave is 1.0 GHz. Both the CRWG and the rotated BC functions are chosen as the testing functions in the discretization of the identity operators. (a) A sphere with a radius of 1.0 m. (b) A cube with a size of $1.0 \times 1.0 \times 1.0$ m^3.

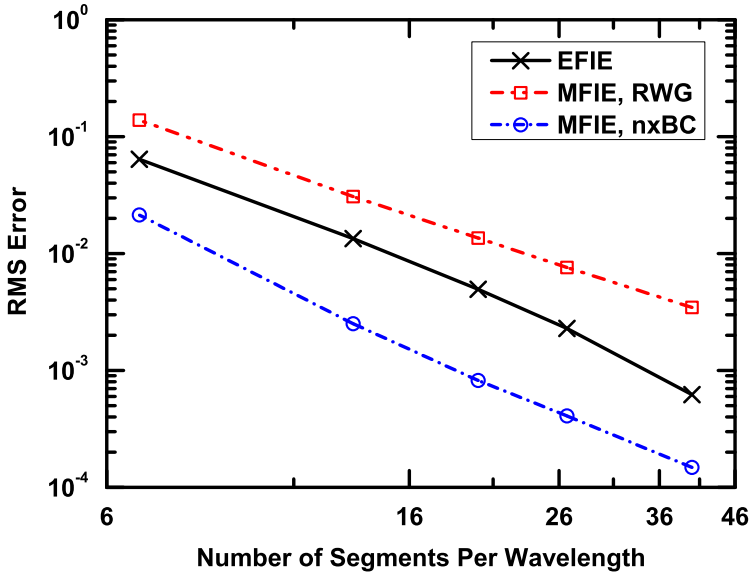

(a)

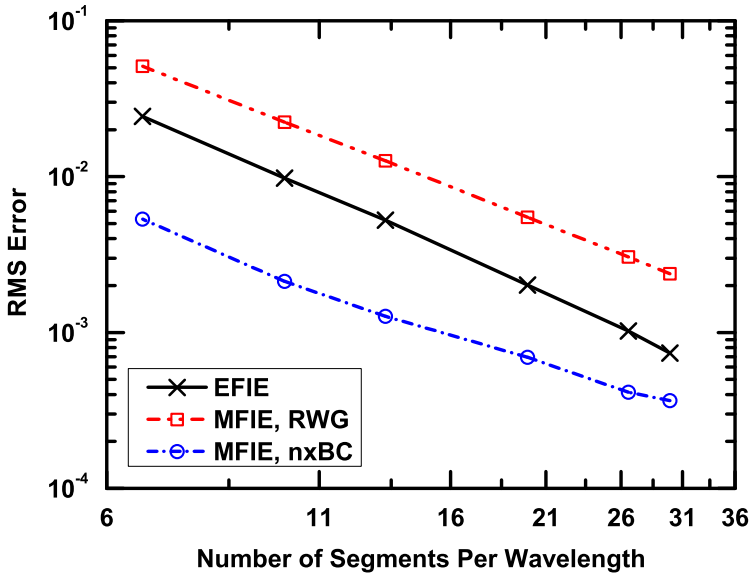

(b)

Figure 3.4: RMS error of the RCS calculated by the MFIE and the EFIE in the PEC case versus discretization density. Both the CRWG testing scheme and the rotated-BC testing scheme of the MFIE are shown and compared with the EFIE. (a) A 75-MHz, V-polarized plane wave is incident on a PEC sphere with a radius of 1.0 m. (b) A 150-MHz, V-polarized plane wave is incident on a PEC sphere with a radius of 1.0 m.

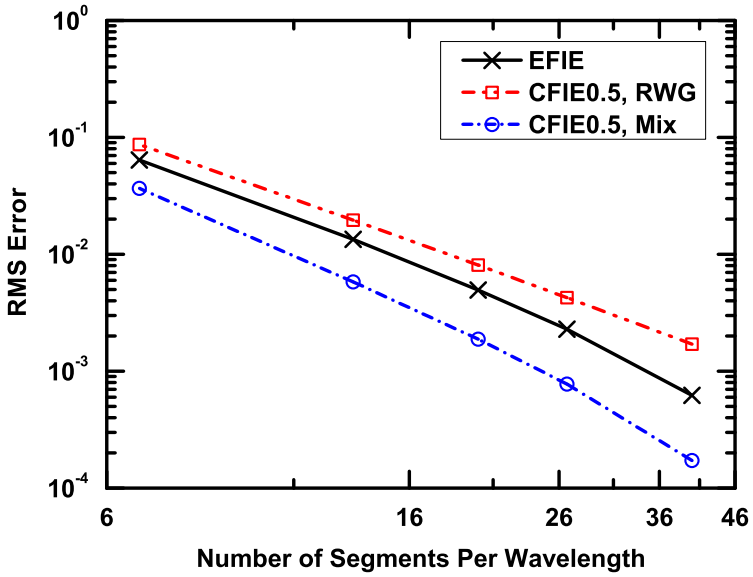

(a)

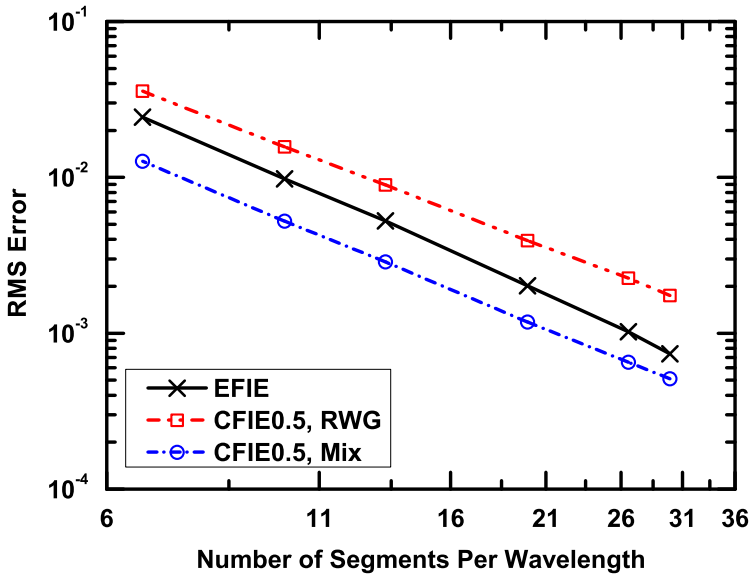

(b)

Figure 3.5: RMS error of the RCS calculated by the CFIE with a combination factor of 0.5 and the EFIE in the PEC case versus discretization density. Both the CRWG testing scheme and the mixed testing scheme of the CFIE are shown and compared with the EFIE. (a) A 75-MHz, V-polarized plane wave is incident on a PEC sphere with a radius of 1.0 m. (b) A 150-MHz, V-polarized plane wave is incident on a PEC sphere with a radius of 1.0 m.

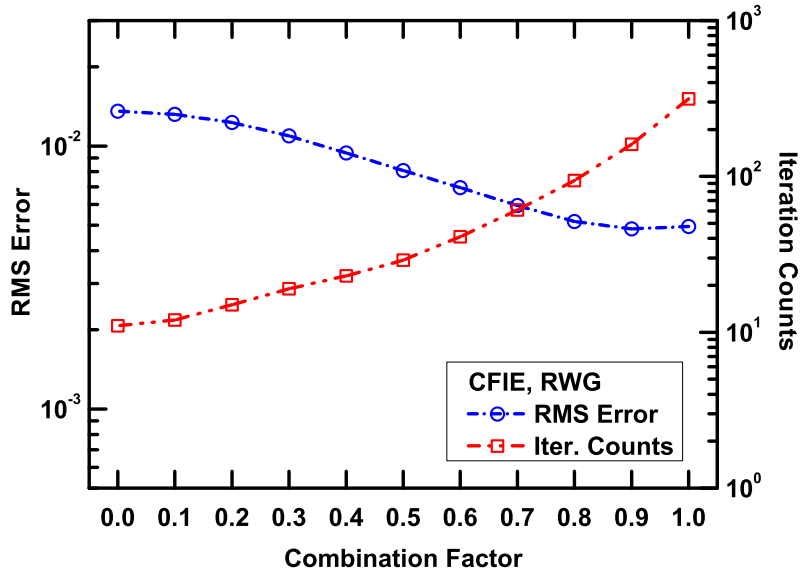

(a)

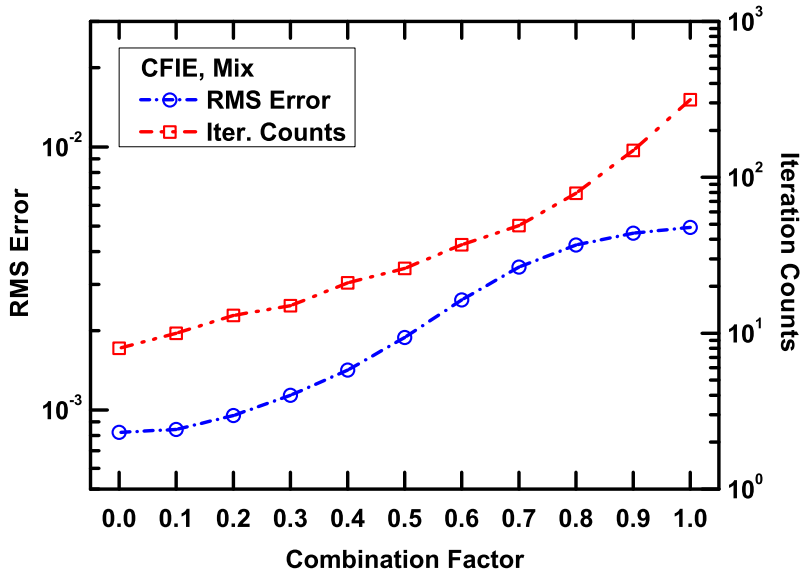

(b)

Figure 3.6: RMS error of the RCS calculated by the CFIE in the PEC case with different discretization schemes and the iteration counts required in the BiCGstab(1) iterative solution to achieve a relative residual error of 10^{-6}, both as a function of the combination factor α. A 75-MHz, V-polarized plane wave is incident on a PEC sphere with a radius of 1.0 m. (a) The CFIE with the CRWG testing scheme. (b) The CFIE with the mixed testing scheme.

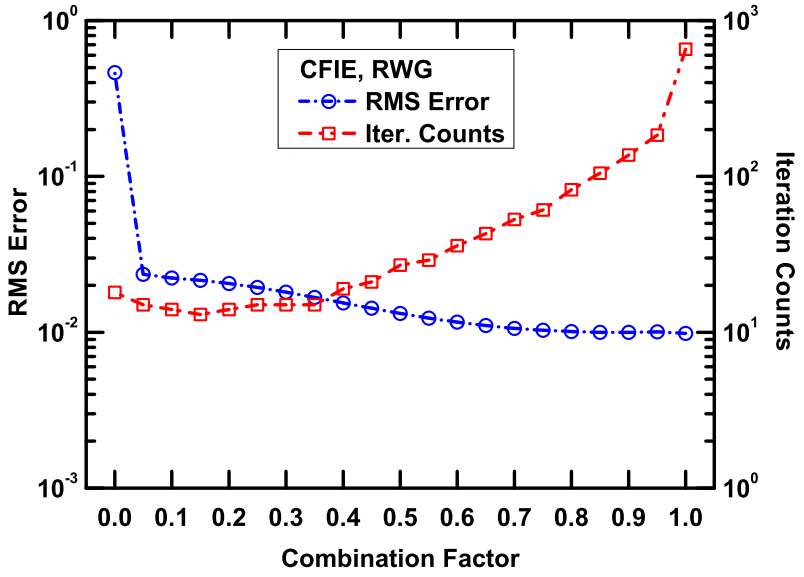

(a)

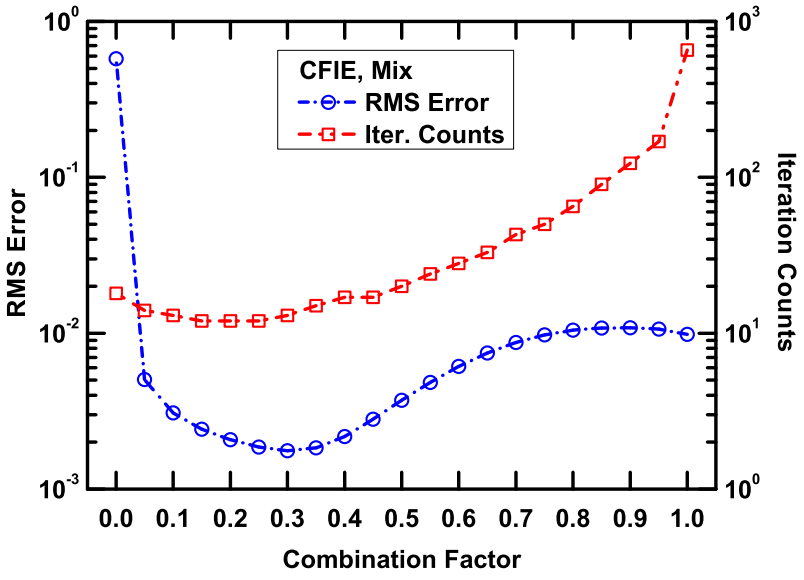

(b)

Figure 3.7: RMS error of the RCS calculated by the CFIE in the PEC case with different discretization schemes and the iteration counts required in the BiCGstab(1) iterative solution to achieve a relative residual error of 10^{-6}, both as a function of the combination factor α. A 131.005-MHz, V-polarized plane wave is incident on a PEC sphere with a radius of 1.0 m. (a) The CFIE with the CRWG testing scheme. (b) The CFIE with the mixed testing scheme.

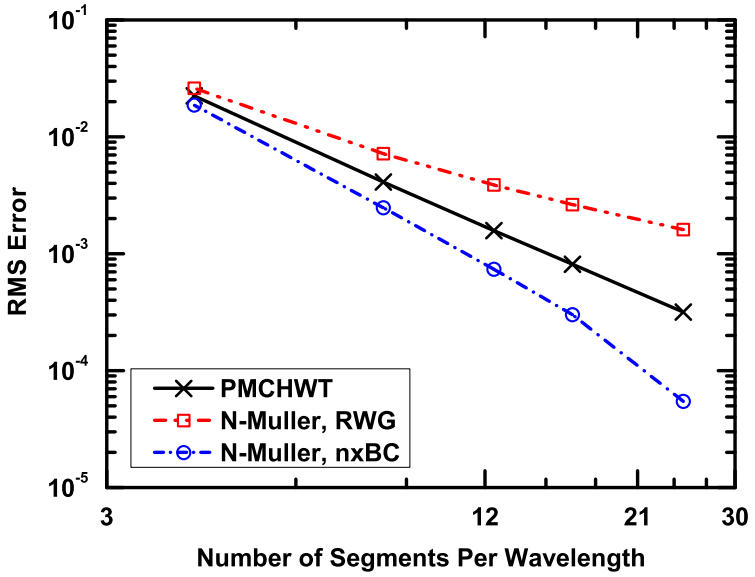

(a)

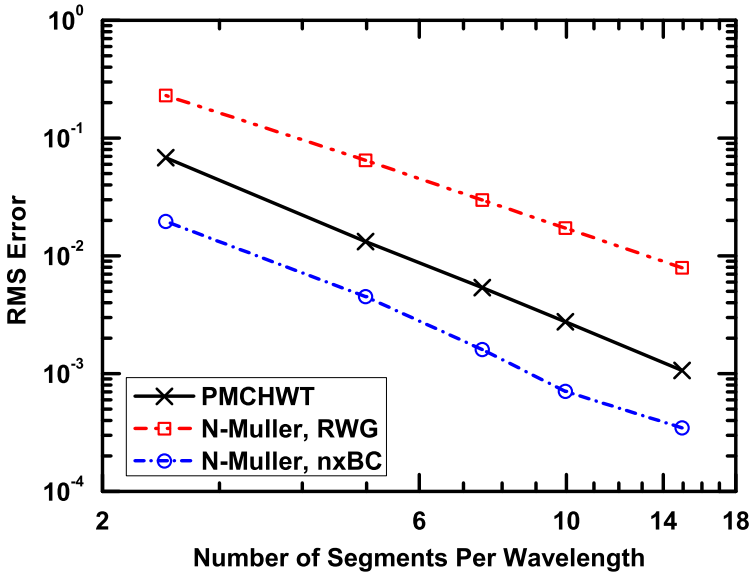

(b)

Figure 3.8: RMS error of the RCS calculated by different SIEs in the dielectric case versus discretization density. Accuracy of the PMCHWT equations and the Müller equations are compared. Both the CRWG testing scheme and the rotated-BC testing scheme of the Müller equations are shown and compared with the PMCHWT equations. (a) A 75-MHz, V-polarized plane wave is incident on a dielectric sphere with a radius of 1.0 m and the dielectric parameters $\varepsilon_r = 2.6$ and $\mu_r = 1.0$. (b) A 100-MHz, H-polarized plane wave is incident on a dielectric sphere with a radius of 1.0 m and the dielectric parameters $\varepsilon_r = 4.0$ and $\mu_r = 1.0$.

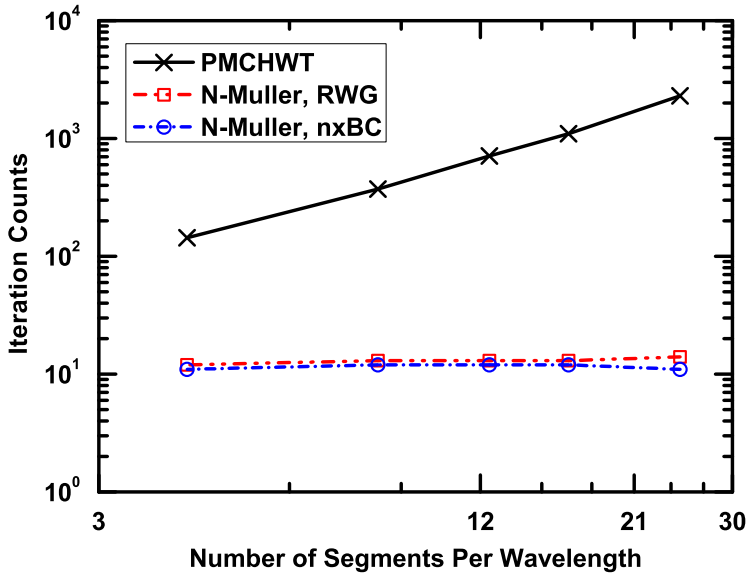

(a)

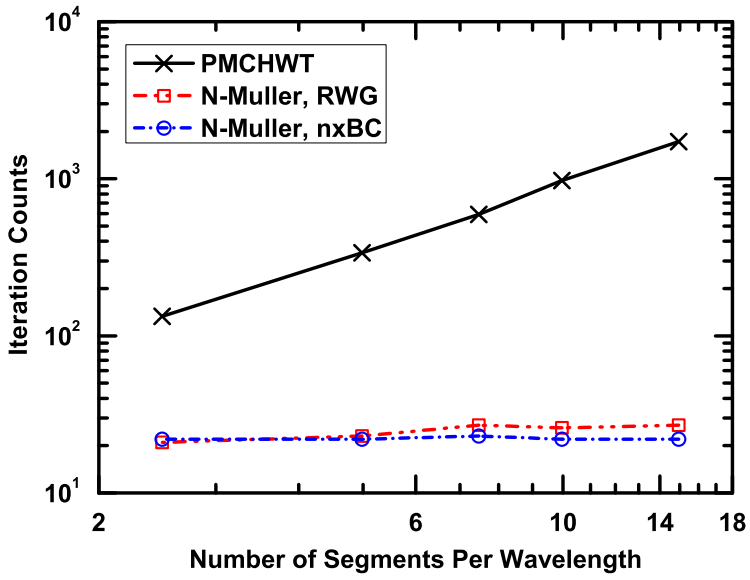

(b)

Figure 3.9: Iteration counts required by different SIEs in the dielectric case versus discretization density. The BiCGstab(1) iterative solver is used to solve the SIEs to a relative residual error of 10^{-6}. (a) A 75-MHz, V-polarized plane wave is incident on a dielectric sphere with a radius of 1.0 m and the dielectric parameters $\varepsilon_r = 2.6$ and $\mu_r = 1.0$. (b) A 100-MHz, H-polarized plane wave is incident on a dielectric sphere with a radius of 1.0 m and the dielectric parameters $\varepsilon_r = 4.0$ and $\mu_r = 1.0$.

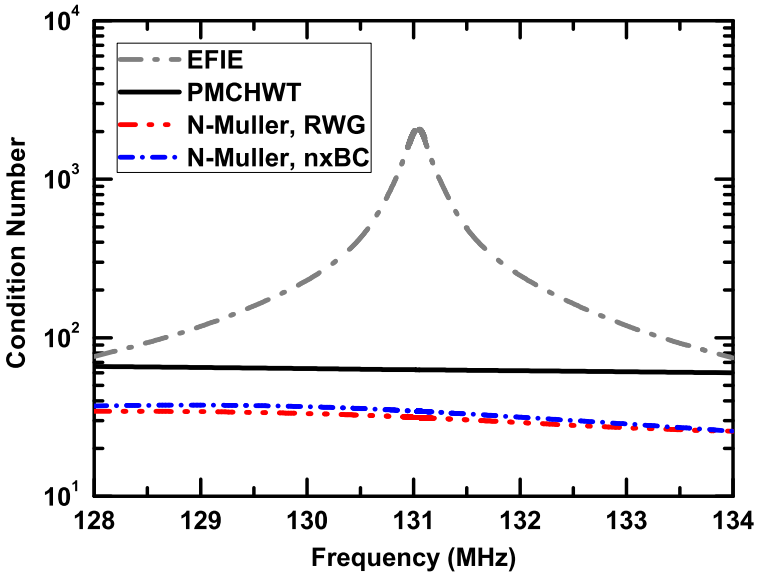

(a)

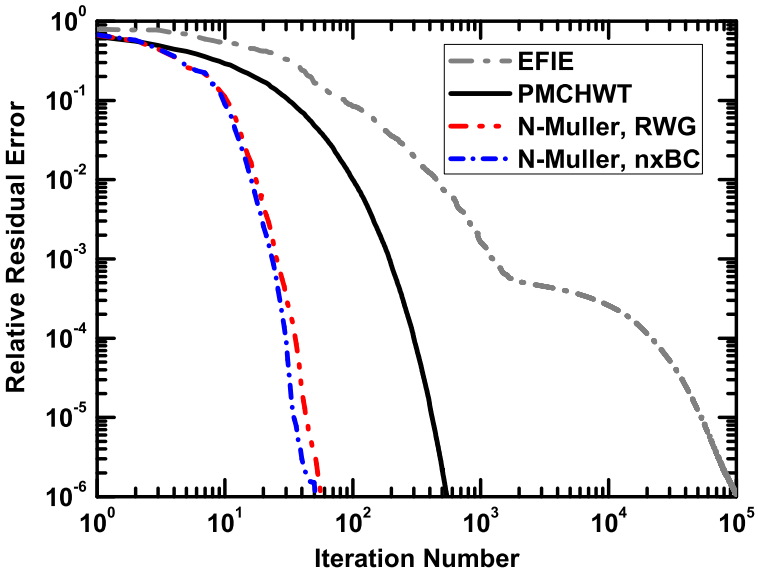

(b)

Figure 3.10: Interior resonance test of the PMCHWT equations, the Müller equations with the RWG testing scheme, and the Müller equations with the rotated-BC testing scheme for scattering analysis of a dielectric sphere with $\varepsilon_r = 4.0$ and $\mu_r = 1.0$. The radius of the sphere is 1.0 m. (a) Condition numbers as a function of the frequency in a small band around the analytical resonant frequency. The condition number of the EFIE for the dielectric case is shown as reference. (b) Convergence histories of different equations to achieve a relative residual error of 10^{-6} at the frequency of 131.036 MHz. The convergence history of the EFIE for the dielectric case is shown as reference.

CHAPTER 4

ACCURACY IMPROVEMENT OF THE SECOND-KIND INTEGRAL EQUATIONS FOR GENERALLY SHAPED OBJECTS

In this chapter, the accuracy improvement by using the BC testing technique is generalized to the solution of electromagnetic problems with generally shaped objects in both the PEC and the dielectric cases. By using the BC functions as the testing functions and by carefully handling the near-singularities associated with both the $\mathcal{K}$ and the $\mathcal{T}$ operators, the numerical accuracy of the second-kind integral equations in the solution to a generally shaped object can be improved significantly. In order to measure the numerical error in solving problems with generally shaped objects, null-field problems are solved, and the root-mean-square (RMS) error of the total field in the far-zone is defined as the numerical error in the solutions of the integral equations. Several numerical examples are given to demonstrate the performance of the proposed techniques in improving the numerical accuracy of the second-kind integral equations.

4.1 Near-Singularity Extraction

As mentioned in the preceding chapters, when discretized using Galerkin's method, where the basis and the testing functions are chosen to be the same, the first-kind integral equations always produce numerical solutions with a much better accuracy than the second-kind integral equations. In this section, the method of handling the near-singularities in the evaluation of the system matrix elements is presented, in order to improve the numerical accuracy of the second-kind integral equations for generally shaped objects.

By using the $\hat{\boldsymbol{n}}\times$ BC testing scheme discussed above, it has been demonstrated in [46] that the numerical accuracy of the second-kind integral equations can be improved by one order of magnitude in the solution of smooth objects. However, the simple application of the $\hat{\boldsymbol{n}}\times$ BC testing scheme is

not sufficient to improve the numerical accuracy of the second-kind integral equations so drastically when generally shaped objects are considered. The major reason is that when generally shaped objects are involved, the $\mathcal{K}$ operator is no longer a compact operator, and the near-field interaction related to the $\mathcal{K}$ operator is no longer weak. As a result, it is necessary to take into account the near-field interaction accurately, in order to further suppress the numerical error in the evaluation of the system matrix elements and improve the accuracy of the final solution.

The singularities, which occur when an observation point $\boldsymbol{r}$ is located in a source patch containing $\boldsymbol{r}'$, are usually extracted by the well-known Duffy's transform [47] for the $\mathcal{T}$ operator, and the Cauchy's principal value integration for the $\mathcal{K}$ operator. In this section, the main issue considered is the so-called near-singularity, which occurs when an observation point $\boldsymbol{r}$ is sufficiently close to a source patch. The near-singularity can be handled using the near-singularity extraction technique. When $\boldsymbol{r}$ falls into a source patch, the near-singularity extraction becomes the singularity extraction automatically.

The discussion begins with the handling of the $\mathcal{K}$ operator. By expanding e^{ikR} in terms of the Taylor series when R is small

$$\begin{aligned} e^{ikR} &= \sum_{m=0}^{\infty} \frac{(ikR)^m}{m!} \\ &= 1 + ikR - \frac{1}{2}k^2R^2 + \mathcal{O}\left(R^3\right) \end{aligned} \tag{4.1}$$

the Green's function and its gradient can be expressed as

$$\frac{e^{ikR}}{R} = \frac{1}{R} + ik - \frac{1}{2}k^2R + \mathcal{O}\left(R^2\right) \tag{4.2}$$

and

$$\begin{aligned} \nabla\frac{e^{ikR}}{R} &= \nabla\frac{1}{R} - \frac{k^2}{2}\nabla R + \mathcal{O}\left(R\right) \\ &= -\frac{\boldsymbol{R}}{R^3} - \frac{k^2}{2}\frac{\boldsymbol{R}}{R} + \mathcal{O}\left(R\right) \end{aligned} \tag{4.3}$$

respectively, where $\boldsymbol{R} = \boldsymbol{r} - \boldsymbol{r}'$. In the evaluation of the system matrix

element (3.6), if we fix the observation point to be $\boldsymbol{r}_0$, (3.6) becomes

$$Z_{mn}^{\mathcal{K}} = \frac{1}{4\pi} \int_{S_m} \boldsymbol{t}_m (\boldsymbol{r}_0) \cdot \hat{\boldsymbol{n}} (\boldsymbol{r}_0) \times \boldsymbol{Z}_{mn}^{\mathcal{K}} (\boldsymbol{r}_0) \, \mathrm{d}\boldsymbol{r}_0 \tag{4.4}$$

where

$$\boldsymbol{Z}_{mn}^{\mathcal{K}} (\boldsymbol{r}_0) = P.V. \int_{S_n} \nabla \frac{e^{ikR_0}}{R_0} \times \boldsymbol{f}_n^r (\boldsymbol{r}') \, \mathrm{d}\boldsymbol{r}' \tag{4.5}$$

is the interior integral over the source parch S_n, and $R_0 = \|\boldsymbol{r}_0 - \boldsymbol{r}'\|$.

When $\boldsymbol{r}_0$ is close to the source patch so that R_0 is small, we can subtract the first two terms in the Taylor series expansion of the gradient of the Green's function (4.3) from the integrand of (4.5), and add them back. By doing so, the near-singularity extraction for the $\mathcal{K}$ operator can be expressed as

$$\begin{aligned}
\boldsymbol{Z}_{mn}^{\mathcal{K}} (\boldsymbol{r}_0) \; &= \; P.V. \int_{S_n} \nabla \frac{e^{ikR_0}}{R_0} \times \boldsymbol{f}_n^r (\boldsymbol{r}') \, \mathrm{d}\boldsymbol{r}' \\
&= \; P.V. \int_{S_n} \Bigg\{ \nabla \frac{e^{ikR_0}}{R_0} \times \boldsymbol{f}_n^r (\boldsymbol{r}') \\
&\quad - \left[\nabla \frac{1}{R_0} - \frac{k^2}{2} \frac{\boldsymbol{R}_0}{R_0} \right] \times \boldsymbol{f}_n^r (\boldsymbol{r}_0) \Bigg\} \mathrm{d}\boldsymbol{r}' \\
&\quad + \; P.V. \left[\boldsymbol{I}_1 - \frac{k^2}{2} \boldsymbol{I}_2 \right] \times \boldsymbol{f}_n^r (\boldsymbol{r}_0)
\end{aligned} \tag{4.6}$$

where

$$\boldsymbol{I}_1 = \int_{S_n} \nabla \frac{1}{R_0} \, \mathrm{d}\boldsymbol{r}' \tag{4.7}$$

$$\boldsymbol{I}_2 = \int_{S_n} \frac{\boldsymbol{R}_0}{R_0} \, \mathrm{d}\boldsymbol{r}'. \tag{4.8}$$

It should be noted that, in the subtracted and added terms in (4.6), $\boldsymbol{f}_n^r (\boldsymbol{r}_0)$ instead of $\boldsymbol{f}_n^r (\boldsymbol{r}')$ is used. When $\boldsymbol{r}_0 = \boldsymbol{r}'$, the integrand of the first integral on the right-hand side of (4.6) becomes zero, because $\boldsymbol{f}_n^r$ becomes the same, and

$$\nabla \frac{e^{ikR_0}}{R_0} - \nabla \frac{1}{R_0} + \frac{k^2}{2} \frac{\boldsymbol{R}_0}{R_0} = \mathcal{O} (R_0) = 0 \tag{4.9}$$

since $R_0 = \|\boldsymbol{r}_0 - \boldsymbol{r}'\| = 0$. When $\boldsymbol{r}_0 \neq \boldsymbol{r}'$, but $\boldsymbol{r}_0 \to \boldsymbol{r}'$, such an integrand becomes well behaved, meaning that after expansion, the denominator and

the numerator are on the same order of magnitude, which preserves a good numerical accuracy upon evaluation.

Similarly, the near-singularity extraction for the $\mathcal{T}$ operator can be expressed as

$$\begin{aligned} Z_{mn}^{\mathcal{T}} &= \frac{ik_j}{4\pi}\int_{S_m}\int_{S_n} F\left(\boldsymbol{r}_0,\boldsymbol{r}'\right)\frac{e^{ikR_0}}{R_0}\mathrm{d}\boldsymbol{r}'\mathrm{d}\boldsymbol{r}_0 \\ &= \frac{ik_j}{4\pi}\int_{S_m}\int_{S_n}\left[F\left(\boldsymbol{r}_0,\boldsymbol{r}'\right)\frac{e^{ikR_0}}{R_0}\right. \\ &\quad \left. - F\left(\boldsymbol{r}_0,\boldsymbol{r}_0\right)\frac{1}{R_0}\right]\mathrm{d}\boldsymbol{r}'\mathrm{d}\boldsymbol{r}_0 \\ &\quad + \frac{ik_j}{4\pi}\int_{S_m} F\left(\boldsymbol{r}_0,\boldsymbol{r}_0\right)\, I_3\, \mathrm{d}\boldsymbol{r}_0 \end{aligned} \tag{4.10}$$

where

$$\begin{aligned} F\left(\boldsymbol{r}_0,\boldsymbol{r}'\right) &= \boldsymbol{f}_m^b\left(\boldsymbol{r}_0\right)\cdot\boldsymbol{f}_n^r\left(\boldsymbol{r}'\right) \\ &\quad -\frac{1}{k_j^2}\nabla\cdot\boldsymbol{f}_m^b\left(\boldsymbol{r}_0\right)\nabla'\cdot\boldsymbol{f}_n^r\left(\boldsymbol{r}'\right) \end{aligned} \tag{4.11}$$

$$\begin{aligned} F\left(\boldsymbol{r}_0,\boldsymbol{r}_0\right) &= \boldsymbol{f}_m^b\left(\boldsymbol{r}_0\right)\cdot\boldsymbol{f}_n^r\left(\boldsymbol{r}_0\right) \\ &\quad -\frac{1}{k_j^2}\nabla\cdot\boldsymbol{f}_m^b\left(\boldsymbol{r}_0\right)\nabla\cdot\boldsymbol{f}_n^r\left(\boldsymbol{r}_0\right) \end{aligned} \tag{4.12}$$

and

$$I_3 = \int_{S_n}\frac{1}{R_0}\,\mathrm{d}\boldsymbol{r}'. \tag{4.13}$$

When $\boldsymbol{r}_0 = \boldsymbol{r}'$, the integrand of the first integral on the right-hand side of (4.10) becomes $ik_j\,F\left(\boldsymbol{r}_0,\boldsymbol{r}_0\right)$. When $\boldsymbol{r}_0 \neq \boldsymbol{r}'$, but $\boldsymbol{r}_0 \to \boldsymbol{r}'$, such an integrand also becomes well behaved, which preserves a good numerical accuracy upon evaluation.

4.2 Analytical Evaluation of Integrals over Planar Triangles

After the near-singularity extraction, the integrands of the first integrals on the right-hand sides of (4.6) and (4.10) are both well defined, which allow ac-

curate numerical integrations to be performed. For $\boldsymbol{I}_1$, $\boldsymbol{I}_2$, and I_3, analytical expressions [48] can be used to evaluate these integrals accurately. For the sake of completeness and the convenience of implementation, these analytical expressions are summarized here. It should be pointed out that, although all expressions can be found in [48], some of them are rewritten here in order to fit into the context more appropriately.

Define a local rectangular coordinate system $(\hat{\boldsymbol{u}}, \hat{\boldsymbol{v}}, \hat{\boldsymbol{w}})$, where $\hat{\boldsymbol{w}} = \hat{\boldsymbol{u}} \times \hat{\boldsymbol{v}}$, and assume that the source triangular patch S_n locates in the u-v plane. The local coordinates of the three vertexes of the triangle are $\boldsymbol{P}_1 = (0, 0, 0)$, $\boldsymbol{P}_2 = (l_3, 0, 0)$, and $\boldsymbol{P}_3 = (u_3, v_3, 0)$, respectively. Under such a coordinate system, the observation point $\boldsymbol{r}_0 = (u_0, v_0, w_0)$. By defining the edge length, the unit edge tangential vectors, and the unit edge normal vectors as $(i = 1, 2, 3)$

$$l_i = \|\boldsymbol{P}_{i-1} - \boldsymbol{P}_{i+1}\| \tag{4.14}$$

$$\hat{\boldsymbol{s}}_i = \frac{\boldsymbol{P}_{i-1} - \boldsymbol{P}_{i+1}}{l_i} \tag{4.15}$$

$$\hat{\boldsymbol{m}}_i = \hat{\boldsymbol{s}}_i \times \hat{\boldsymbol{w}} \tag{4.16}$$

respectively, and other auxiliary variables as follows

$$\begin{aligned}
S_1^+ &= \frac{(u_3 - u_0)(u_3 - l_3) + v_3(v_3 - v_0)}{l_1} \\
S_1^- &= -\frac{(l_3 - u_0)(l_3 - u_3) + v_0 v_3}{l_1} \\
S_2^+ &= \frac{u_0 u_3 + v_0 v_3}{l_2} \\
S_2^- &= -\frac{u_3(u_3 - u_0) + v_3(v_3 - v_0)}{l_2} \\
S_3^+ &= l_3 - u_0 \\
S_3^- &= -u_0 \\
t_1^0 &= \frac{v_0(u_3 - l_3) + v_3(l_3 - u_0)}{l_1} \\
t_2^0 &= \frac{u_0 v_3 - v_0 u_3}{l_2} \\
t_3^0 &= v_0 \\
t_1^+ &= \sqrt{(u_3 - u_0)^2 + (v_3 - v_0)^2} \\
t_1^- &= \sqrt{(l_3 - u_0)^2 + v_0^2} \\
t_2^+ &= \sqrt{u_0^2 + v_0^2}
\end{aligned}$$

$$
\begin{aligned}
t_2^- &= t_1^+ \\
t_3^+ &= t_1^- \\
t_3^- &= t_2^+ \\
R_i^0 &= \sqrt{\left(t_i^0\right)^2 + w_0^2} \\
R_i^\pm &= \sqrt{\left(t_i^\pm\right)^2 + w_0^2}
\end{aligned}
$$

the analytical expressions for $\boldsymbol{I}_1$, $\boldsymbol{I}_2$, and I_3 can be expressed as

$$\boldsymbol{I}_1 = -\hat{\boldsymbol{w}}\,\mathrm{sgn}(w_0)\,\beta - \sum_{i=1}^{3} \hat{\boldsymbol{m}}_i\, f_{1i} \tag{4.17}$$

$$\boldsymbol{I}_2 = \hat{\boldsymbol{w}}\, w_0\, I_3 - \frac{1}{2}\sum_{i=1}^{3} \hat{\boldsymbol{m}}_i\, f_{2i} \tag{4.18}$$

$$I_3 = -|w_0|\,\beta + \sum_{i=1}^{3} t_i^0\, f_{1i} \tag{4.19}$$

where "sgn" in (4.17) stands for the sign function, and

$$\begin{aligned}
\beta \;=\; \sum_{i=1}^{3} \Bigg[&\arctan \frac{t_i^0 S_i^+}{\left(R_i^0\right)^2 + |w_0| R_i^+} \\
&- \arctan \frac{t_i^0 S_i^-}{\left(R_i^0\right)^2 + |w_0| R_i^-} \Bigg]
\end{aligned} \tag{4.20}$$

$$f_{1i} \;=\; \ln\left(\frac{R_i^+ + S_i^+}{R_i^- + S_i^-}\right) \tag{4.21}$$

$$f_{2i} \;=\; \left(S_i^+ R_i^+ - S_i^- R_i^-\right) + \left(R_i^0\right)^2 f_{1i}. \tag{4.22}$$

When $\boldsymbol{r}_0$ locates in the u-v plane, $w_0 = 0$, and

$$P.V.\ \boldsymbol{I}_1(w_0 = 0) = -\sum_{i=1}^{3} \hat{\boldsymbol{m}}_i\, f_{1i}(w_0 = 0) \tag{4.23}$$

$$P.V.\ \boldsymbol{I}_2(w_0 = 0) = -\frac{1}{2}\sum_{i=1}^{3} \hat{\boldsymbol{m}}_i\, f_{2i}(w_0 = 0) \tag{4.24}$$

$$I_3(w_0 = 0) = \sum_{i=1}^{3} t_i^0\, f_{1i}(w_0 = 0) \tag{4.25}$$

can be used for the singularity extraction.

By applying the techniques presented in these two sections, the near-singularities in the $\mathcal{K}$ and the $\mathcal{T}$ operators can be handled and evaluated accurately. In the following sections, numerical examples will be given by using all the techniques introduced here.

4.3 Numerical Examples: The PEC Case

In this section, the accuracy of the first- and the second-kind integral equations in both the PEC case are investigated and compared, using the testing schemes and near-singularity extraction technique discussed in Section 4.1. In order to evaluate the numerical errors in the solutions of the generally shaped objects accurately, the null-field problems instead of the scattering problems are solved, and (2.30)-(2.35) are used in the measurement of numerical errors. The incident fields in the null-field problems come from the radiation of a vertically oriented infinitesimal Hertzian dipole at the center of the objects in all numerical examples

$$\begin{aligned} \boldsymbol{E}^{\text{inc}}(\boldsymbol{r}) &= -\hat{\boldsymbol{\theta}}\,\frac{ik\eta\sin\theta}{4\pi r}\left[1-\frac{1}{ikr}-\frac{1}{(kr)^2}\right]e^{ikr} \\ &\quad +\hat{\boldsymbol{r}}\,\frac{\eta\cos\theta}{2\pi r^2}\left(1-\frac{1}{ikr}\right)e^{ikr} \qquad (4.26) \\ \boldsymbol{H}^{\text{inc}}(\boldsymbol{r}) &= -\hat{\boldsymbol{\phi}}\,\frac{ik\sin\theta}{4\pi r}\left(1-\frac{1}{ikr}\right)e^{ikr}. \qquad (4.27) \end{aligned}$$

For all integral equations solved in this section, the near-singularities are handled properly using the technique discussed in the preceding section, in order to have a fair comparison.

The first- and the second-kind integral equations for the null-field problems in the PEC case are the EFIE (2.26) and the MFIE (2.27), respectively. Calculations are performed for several geometries, including a cube, a tetrahedron, a rectangular pyramid, and a pentagonal prism.

4.3.1 Cube

The first object considered here is a PEC cube with the edge length of 2.0 m, under the excitation of a 300-MHz incident wave. Figure 4.1 shows the

numerical accuracy of the EFIE and those of the MFIE with two different testing schemes versus the geometrical mesh density. Evidently, by using the RWG functions as the testing functions, the MFIE produces numerical solutions with larger errors than the EFIE, as has been commonly observed. However, when the $\hat{\boldsymbol{n}}\times$ BC functions are employed as the testing functions, the MFIE gives a much smaller error, even smaller than that of the EFIE.

4.3.2 Tetrahedron

The second object is a tetrahedron, which has a circumscribed sphere with the radius of 2.0 m. The frequency of the incident wave is 300 MHz. The RMS errors of three different equations are shown in Figure 4.2. A similar observation to that in the cube example can be obtained. The reason for a steeper decrease of the RMS error from the first mesh point to the second mesh point is because at the first mesh point, the mesh density is too low for the basis functions to describe the edge singularity of the induced currents well.

4.3.3 Rectangular Pyramid

Next, a very sharp object, which is a PEC rectangular pyramid, is considered to demonstrate the capability of the proposed method in handling the sharp tips. The base of this object is a rectangle with a size of 1.0 m by 1.0 m, and the height of the pyramid is 4.0 m. The frequency of the incident wave is also 300 MHz. Figure 4.3 shows the numerical results. With sufficiently dense geometrical discretizations, the edge and tip singularity of the induced currents can be described properly. It is very clear that, using the proposed $\hat{\boldsymbol{n}}\times$ BC testing scheme along with the near-singularity extraction technique, the numerical accuracy of the MFIE can be improved by nearly one order of magnitude, and is much better than that of the EFIE.

4.3.4 Pentagonal Prism

The last example for the PEC case is the null-field problem of a pentagonal prism under the excitation of a 300-MHz incident wave. The geometry

and the numerical results are shown in Fig. 4.4. The base is a pentagon, whose circumradius is 1.0 m, and the height of the prism is 2.0 m. Two observations can be made from this figure. First, as is observed from the preceding examples, applying the proposed techniques can improve the numerical accuracy of the MFIE significantly, making it even better than the EFIE, which is traditionally known to have a much better accuracy. Second, the convergence rate of the RMS error of the EFIE becomes slower when the mesh density increases. This is because when the mesh is refined, the system matrix produced by discretizing the EFIE will have an increased condition number. According to the basic knowledge of the numerical analysis, when the condition number of a matrix becomes too large, the matrix equation system becomes very sensitive to the numerical errors in the evaluation of the matrix elements as well as the right-hand side vector elements; therefore, the solution accuracy will be deteriorated. This phenomenon can be seen more clearly in the examples in the dielectric case.

Generally speaking, from the examples shown here, it can be concluded that in the PEC case, when the MFIE is solved using the proposed techniques, its numerical accuracy can be improved by 5 to 10 times over the traditional solution scheme, and is better than that of the EFIE.

4.4 Numerical Examples: The Dielectric Case

The first- and the second-kind integral equations for the null-field problems in the dielectric case are the PMCHWT equations (2.28) and the Müller equations (2.29), respectively. In this section, dielectric objects in the shape of a cube, a tetrahedron, and a rectangular pyramid are considered. The geometry sizes of these objects are exactly the same as those presented in the PEC case.

4.4.1 Cube

First, a dielectric cube with $\varepsilon_r = 2.0$ and $\mu_r = 1.0$ is solved under the excitation of a 300-MHz incident wave. Using the PMCHWT equations, the Müller equations with the RWG testing scheme, and the Müller equations with the $\hat{\boldsymbol{n}}\times$ BC testing scheme, the total electric field in the far zone is

calculated, and the numerical errors due to the solution of these equations are evaluated by (2.35). The RMS errors versus the geometrical mesh density are shown in Figure 4.5. Clearly, the Müller equations with the $\hat{\boldsymbol{n}}\times$ BC testing scheme produces numerical solutions with the best accuracy, much better than the other two equations. The numerical accuracy of the PMCHWT equations is greatly deteriorated when the mesh density is increased, due to the sharp increase of the condition number of its system matrix. In the meantime, the RMS errors of the two Müller equations are both in straight lines, showing the good and stable condition number of the Müller equations, which is not affected by the mesh density.

4.4.2 Tetrahedron

The second example given in the dielectric case is the null-field problem for a dielectric tetrahedron with $\varepsilon_r = 4.0$ and $\mu_r = 1.0$. The frequency of the incident wave is 300 MHz. The RMS errors of the far-field calculations obtained from three equations are shown in Figure 4.6. Again, the Müller equations with the $\hat{\boldsymbol{n}}\times$ BC testing scheme produce numerical solutions with the best accuracy. The numerical accuracy of the PMCHWT equations is not only worse than the Müller equations with the proposed technique, but also deteriorated by the increase of the geometrical mesh density. The RMS errors of the two Müller equations stay in straight lines, showing the robustness of the Müller equations with respect to the mesh density.

4.4.3 Rectangular Pyramid

For the last numerical example, the rectangular pyramid is considered again, in order to show the capability of the Müller equations with the proposed techniques in handling the geometry with very sharp tips. Under the excitation of a 300-MHz incident wave, this dielectric pyramid has a relative permittivity $\varepsilon_r = 4.0$ and a relative permeability $\mu_r = 1.0$. Similar observations can be made from Figure 4.7. The Müller equations with the proposed techniques have the best numerical accuracy among the three equations investigated. It can be seen that when the mesh density comes to about 10 segments per wavelength, the numerical accuracy of the Müller equations

with the $\hat{\boldsymbol{n}}\times$ BC testing scheme is more than 10 times better than the Müller equations with the traditional RWG testing scheme, and also significantly better than that of the PMCHWT equations.

4.5 Summary

In this chapter, the $\hat{\boldsymbol{n}}\times$ BC function is shown to be a better testing function for the discretization of the second-kind integral equations for generally shaped objects. A near-singularity extraction technique is presented and applied for both the $\mathcal{K}$ and the $\mathcal{T}$ operators, in order to reduce the numerical error in the evaluation of the system matrix elements. To measure the numerical errors in the solution of generally shaped objects accurately, the null-field problems are presented and the RMS of the total electric field in the far-zone is defined as the numerical error according to the extinction theorem. It has been shown, from the numerical examples in both the PEC and the dielectric cases, that the proposed techniques are able to reduce the numerical errors of the second-kind integral equations significantly, leading to accurate numerical solutions that are comparable to (or even better than) the existing solutions of their first-kind counterparts in solving problems with generally shaped objects.

4.6 Figures

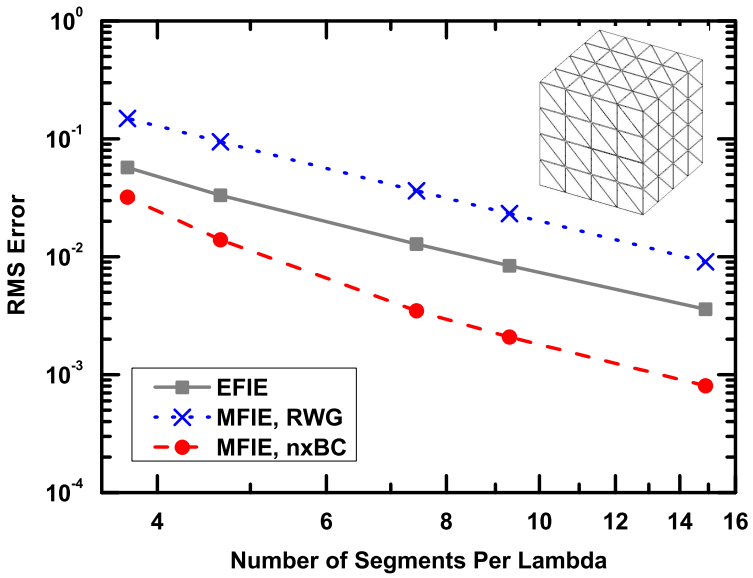

Figure 4.1: Comparison of the numerical accuracy of the EFIE and those of the MFIE with two different testing schemes versus the geometrical mesh density in the solution of a null-field problem for a PEC cube under the excitation of a 300-MHz incident wave.

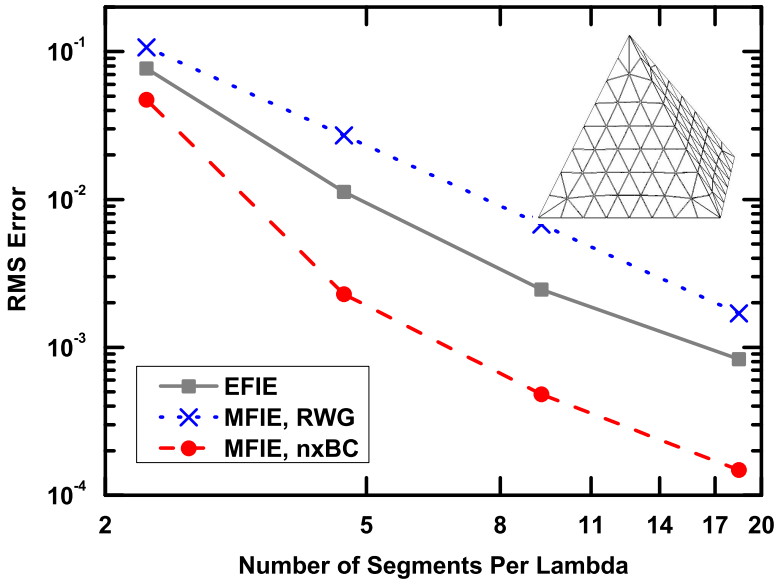

Figure 4.2: Comparison of the numerical accuracy of the EFIE and those of the MFIE with two different testing schemes versus the geometrical mesh density in the solution of a null-field problem for a PEC tetrahedron under the excitation of a 300-MHz incident wave.

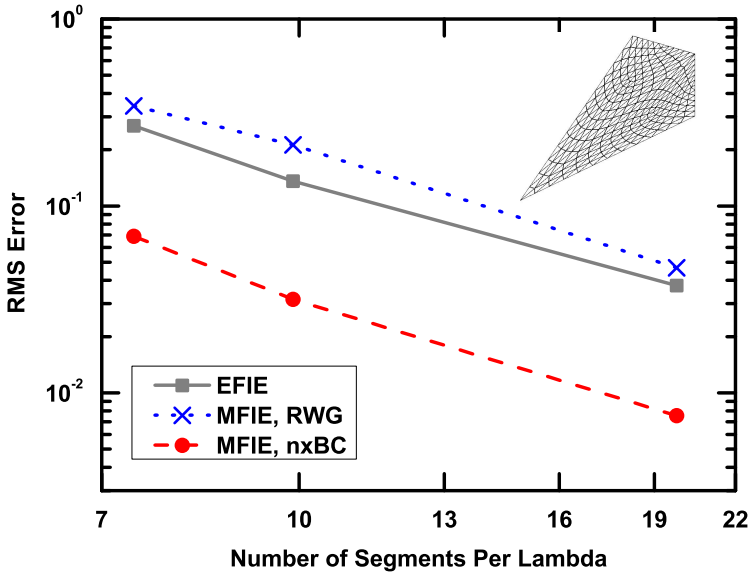

Figure 4.3: Comparison of the numerical accuracy of the EFIE and those of the MFIE with two different testing schemes versus the geometrical mesh density in the solution of a null-field problem for a PEC rectangular pyramid under the excitation of a 300-MHz incident wave.

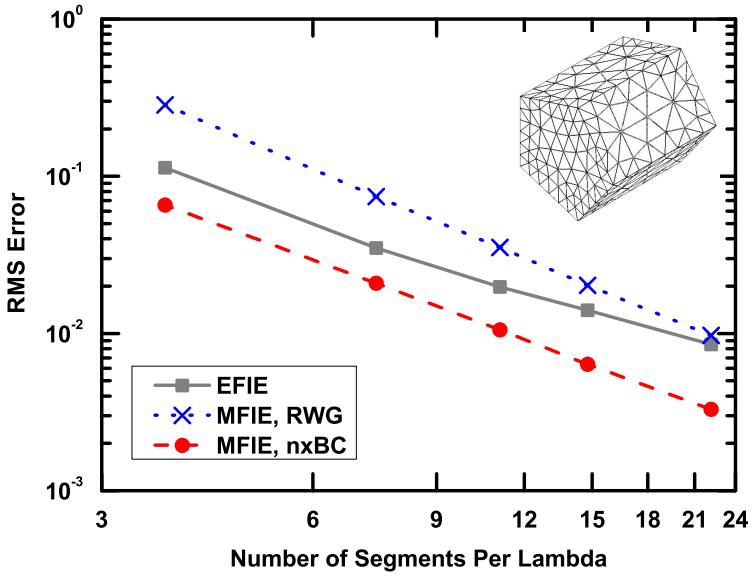

Figure 4.4: Comparison of the numerical accuracy of the EFIE and those of the MFIE with two different testing schemes versus the geometrical mesh density in the solution of a null-field problem for a PEC pentagonal prism under the excitation of a 300-MHz incident wave.

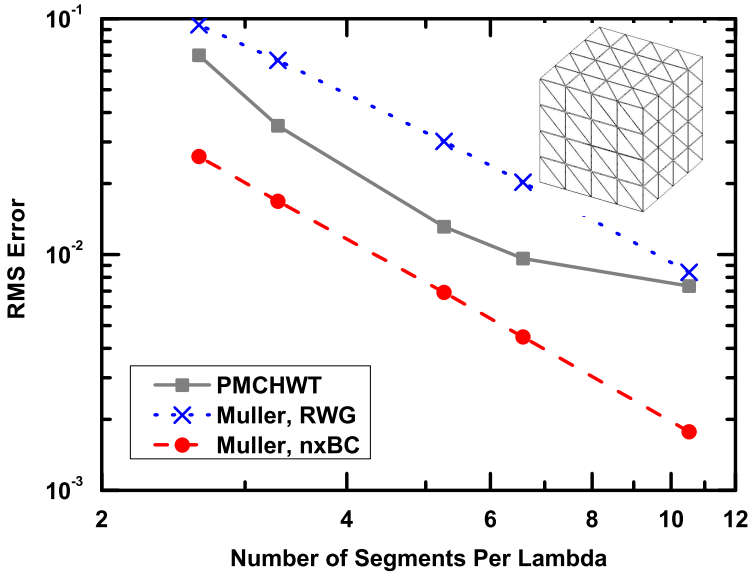

Figure 4.5: Comparison of the numerical accuracy of the PMCHWT equations and those of the Müller equations with two different testing schemes versus the geometrical mesh density in the solution of a null-field problem for a dielectric cube with $\varepsilon_r = 2.0$, $\mu_r = 1.0$, under the excitation of a 300-MHz incident wave.

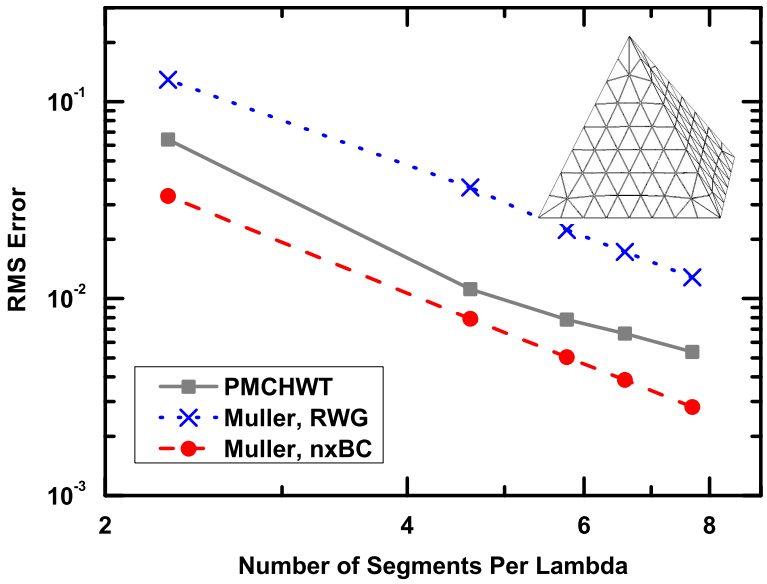

Figure 4.6: Comparison of the numerical accuracy of the PMCHWT equations and those of the Müller equations with two different testing schemes versus the geometrical mesh density in the solution of a null-field problem for a dielectric tetrahedron with $\varepsilon_r = 4.0$, $\mu_r = 1.0$, under the excitation of a 300-MHz incident wave.

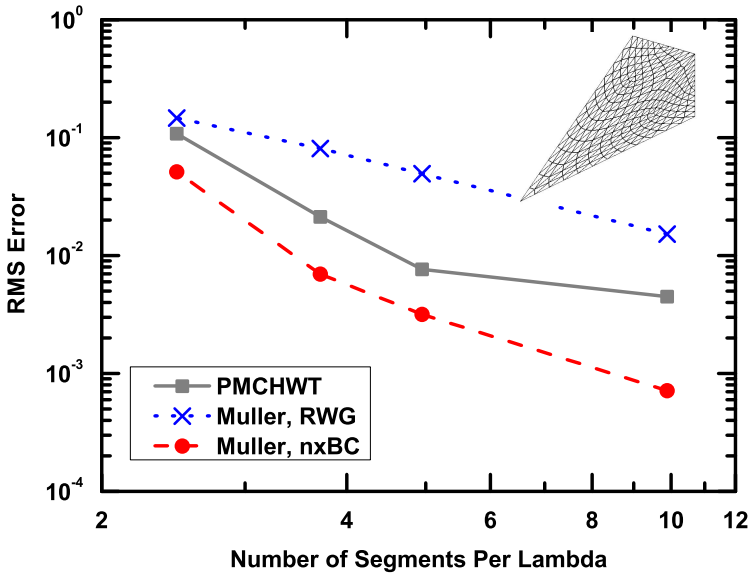

Figure 4.7: Comparison of the numerical accuracy of the PMCHWT equations and those of the Müller equations with two different testing schemes versus the geometrical mesh density in the solution of a null-field problem for a dielectric rectangular pyramid with $\varepsilon_r = 4.0$, $\mu_r = 1.0$, under the excitation of a 300-MHz incident wave.

CHAPTER 5

DISCUSSION

From the theoretical investigation and the numerical demonstration provided in the preceding chapters, it is very clear that by using the proposed techniques, the accuracy of the second-kind integral equations, both in PEC and dielectric cases, can be improved by orders of magnitude. In this chapter, the reasons for the accuracy improvement by the proposed techniques are discussed, and some important concluding remarks are given to clarify several issues related to the accuracy of the integral equations.

5.1 Accuracy of the Identity Operator

As was shown in Section 3.3, the discretization error due to the identity operator, which is shown in [22] to be the major error source of the solution to a second-kind integral equation, is significantly suppressed by the rotated-BC testing scheme. This is obviously the most important reason for the accuracy improvement.

5.2 Implicit Rayleigh-Ritz Scheme

The accuracy improvement can also be attributed to the appropriate adoption of the Rayleigh-Ritz scheme [21]. As a result of the variational method, it is well known that the Rayleigh-Ritz scheme can minimize the physical quantities such as the energy or reaction; therefore, the scheme is able to stabilize the numerical solution [49]. In [21], it was shown that when the CRWG function $\boldsymbol{f}^r$ is employed as the basis function, a Rayleigh-Ritz scheme can be constructed for the MFIE by choosing the $\hat{\boldsymbol{n}} \times \boldsymbol{f}^r$ as the testing function. Unfortunately, this explicit way of constructing the Rayleigh-Ritz scheme

results in an ill-conditioned system matrix which is difficult to solve accurately. The proposed discretization scheme in this thesis can also be regarded as the Rayleigh-Ritz scheme in an implicit sense. In fact, if we notice that both the CRWG function $\boldsymbol{f}^r$ and the BC function $\boldsymbol{f}^b$ can be expressed as the linear superposition of the CRWG functions $\boldsymbol{g}$ defined on the barycentric refinement of the original curvilinear triangular mesh

$$\boldsymbol{f}^r = \sum_{i=0}^{13} c_i \boldsymbol{g}_i \tag{5.1}$$

$$\boldsymbol{f}^b = d_0 \boldsymbol{g}_0 + \sum_{j=1}^{2N_d-1} d_j \boldsymbol{g}_j + d_{\tilde{0}} \boldsymbol{g}_{\tilde{0}} + \sum_{\tilde{j}=1}^{2\tilde{N}_d-1} d_{\tilde{j}} \boldsymbol{g}_{\tilde{j}} \tag{5.2}$$

where the definitions of the weighting factors c_i, d_j, $d_{\tilde{j}}$, and N_d, $\tilde{N}_d$ can be found in [28], then the MFIE system matrix $\bar{\boldsymbol{Z}}$ obtained by using $\boldsymbol{f}^r$ as the basis function and $\hat{\boldsymbol{n}} \times \boldsymbol{f}^b$ as the testing function can be expressed as

$$\bar{\boldsymbol{Z}} = \bar{\boldsymbol{P}}^T \bar{\boldsymbol{Z}}_{\text{bary}} \bar{\boldsymbol{R}} \tag{5.3}$$

where $\bar{\boldsymbol{R}}$ and $\bar{\boldsymbol{P}}$ stand for the transformation matrices mapping from the CRWG functions $\boldsymbol{f}^r$ and the BC functions $\boldsymbol{f}^b$ defined on the original mesh to the CRWG functions $\boldsymbol{g}$ defined on the barycentric refinement, while their columns are composed by cs in (5.1) and ds in (5.2), respectively, and $\bar{\boldsymbol{Z}}_{\text{bary}}$ is the MFIE system matrix obtained on the barycentric refinement by using $\boldsymbol{g}$ as the basis function and $\hat{\boldsymbol{n}} \times \boldsymbol{g}$ as the testing function. Evidently, $\bar{\boldsymbol{Z}}_{\text{bary}}$ is the Rayleigh-Ritz discretization of the MFIE on the barycentric refinement according to [21], while $\bar{\boldsymbol{R}}$ and $\bar{\boldsymbol{P}}$ are nothing but some geometric relations between the original mesh and its barycentric refinement. As a result, $\bar{\boldsymbol{Z}}$ is shown to be the linear combination of the rows and columns of $\bar{\boldsymbol{Z}}_{\text{bary}}$ with some weighting factors defined in $\bar{\boldsymbol{R}}$ and $\bar{\boldsymbol{P}}$. Since $\bar{\boldsymbol{Z}}_{\text{bary}}$ is obtained from the explicit Rayleigh-Ritz scheme, as its linear combination, $\bar{\boldsymbol{Z}}$ can be regarded as the implicit Rayleigh-Ritz discretization of the MFIE, and therefore is able to minimize the functional and stabilize the solution.

5.3 The Method of Weighted Residuals

As is well known, the method of moments is one of the various forms of the method of weighted residuals (MWR) [29], which unifies many approximate methods of solution to the operator equation

$$\mathcal{F}(x) = g \tag{5.4}$$

where $\mathcal{F}$ stands for either a differential or an integral operator and g stands for the known right-hand side. Once the unknown function x, which has an infinite number of degrees of freedom, is approximated (expanded) by the superposition of a set of basis functions $x \approx \sum_{i=1}^{N} a_i \tilde{x}_i$, which only has a finite number of degrees of freedom a_i, the residual due to this model order reduction

$$R = g - \mathcal{F}\left(\sum_{i=1}^{N} a_i \tilde{x}_i\right) \tag{5.5}$$

is minimized by enforcing its inner products with a set of testing (weighting) functions w_j to be zero. Different choices of the testing functions result in different methods, such as the collocation method, the sub-domain method, the least squares method, and Galerkin's method. Clearly, the testing functions serve as the constraints under which the residual is minimized. Therefore, the choice of the testing function is crucial to the optimal approximation of the unknown function.

In the discretization of the identity operator, if the RWG functions are chosen to approximate the unknown electric current $\boldsymbol{J}$ or the unknown magnetic current $\boldsymbol{M}$, both the RWG themselves and the $\hat{\boldsymbol{n}}\times$ BC functions can be used as the testing functions, because they both lie in the same direction as that of the basis functions. However, a closer look at the testing procedure, which is simply the inner product between a basis and a testing function, reveals more mathematical insight. Given a specific basis function, Figure 5.1 shows that there are two different constraints provided by the RWG testing functions. The first constraint assembles 1 entry into the constraint equations, and the second one assembles 4 entries. As a result, the unknown coefficient a_i of a given basis function is enforced (measured) by 5 conditions. When the $\hat{\boldsymbol{n}}\times$ BC function is used as the testing function, due to its unique defi-

nition domain, much more constraints are enforced. As illustrated in Figure 5.2, there are six types of constraints with different constraint intensities imposed on each basis function, resulting in a total of 19 (in the case of an ideal triangulation of the geometry where every triangle is equilateral) constraint conditions (measurements) to each of the unknown coefficient a_i.

Figures 5.3a and 5.3b demonstrate the sparse patterns of the system matrices obtained by discretizing the identity operator using RWG and $\hat{\boldsymbol{n}}\times$ BC as the testing functions, respectively. Defined on the triangulation of a sphere, there are 120 RWG basis functions in total, resulting in a 120-by-120 system matrix from the discretization of the identity operator. The nonzero entries of the matrices are shown by dots in these figures, each column of which represents the constraints imposed by several testing functions. It is very clear from these figures that the $\hat{\boldsymbol{n}}\times$ BC testing scheme gives much more constraints than the RWG testing scheme, which leads to a more accurate approximation to the unknown function, as can be seen in the numerical experiments shown in Section 3.3.

5.4 The Near-Singularity Extraction

Since the major error source of the second-kind integral equations is suppressed by using the $\hat{\boldsymbol{n}}\times$ BC as the testing functions, the other error sources become important in the accurate solution of problems with generally shaped objects.

The reason why the handling of near-singularity can improve the accuracy of the second-kind integral equations for generally shaped objects can be explained as follows. According to (3.6) and the analysis therein, the $\mathcal{K}$ operator is a compact operator only when the surface of an object is smooth; when the surface is not smooth, but has some geometrical edges, corners, or tips on it, the $\mathcal{K}$ operator is not a compact operator anymore. When $\mathcal{K}$ is a compact operator, the near-field interaction between a source and an observation patch is very small compared to the interaction imposed by the $\mathcal{I}$ operator in a second-kind integral equation. However, for those source and observation patches corresponding to the geometrical non-smoothness, their near-field interactions become significant. As a result, the numerical accuracy can only be guaranteed if such near-field interactions are taken into

account accurately.

5.5 Concluding Remarks

From all the techniques, the discussions, and the numerical examples presented in Chapters 3 and 4, several important conclusive observations can be made.

1. The numerical accuracy of the second-kind integral equations can be improved significantly without the change of basis functions which determine the order of accuracy in the approximation of the unknown surface currents. The increase of the order of the basis functions can certainly improve the accuracy of the numerical solutions, as suggested by several research works. But even with the same set of basis functions as used in the first-kind integral equations, the numerical accuracy of the second-kind integral equations can be improved remarkably with the appropriate choice of the testing functions (testing scheme).

2. According to our numerical experiments, the modification of the solid angle expression does not affect the numerical accuracy of the second-kind integral equations much. The reason is quite obvious, because when testing is performed, the quadrature points of the testing functions are always chosen to be located inside a mesh element (a triangular patch, for example). As a result, 2π is always an appropriate choice for the solid angle. Therefore, in all the descriptions, the discussions, and the numerical examples presented in this thesis, the solid angle is always fixed as 2π.

3. The second most important issue related to the accuracy of the second-kind integral equations is the near-singularity in the evaluation of system matrix elements for both the $\mathcal{K}$ and the $\mathcal{T}$ operators. The reason and necessity have been discussed in the preceding section.

4. For the first-kind integral equations, the numerical accuracy will be deteriorated by the increase of the condition numbers of the system matrices when the geometrical discretization density increases, which makes the convergence curves of the RMS errors no longer straight

lines as can be seen very clearly from the numerical examples. In the meantime, the convergence curves of the second-kind integral equations always maintain straight, because the condition numbers of their system matrices remain almost the same regardless of the discretization density.

5.6 Figures

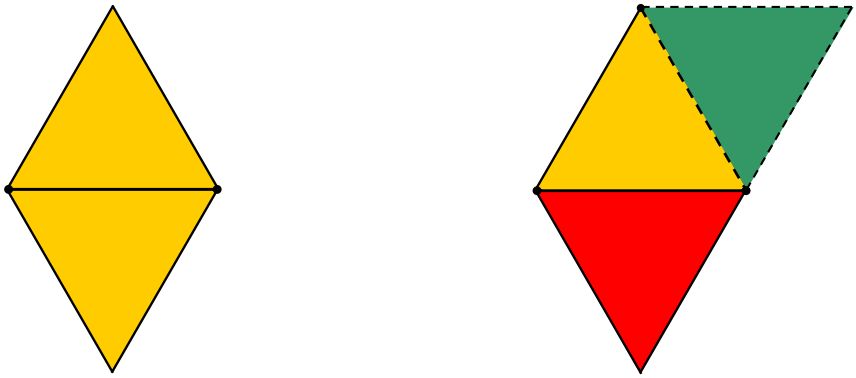

(a) (b)

Figure 5.1: Testing of a RWG basis function with a RWG testing function. The basis function is shown in red, the testing function is shown in green, and their intersection, where the inner product (test) is actually carried out, is shown in yellow. The different cases provide (a) 1 and (b) 4 constraint conditions (measurements) to the basis function, respectively.

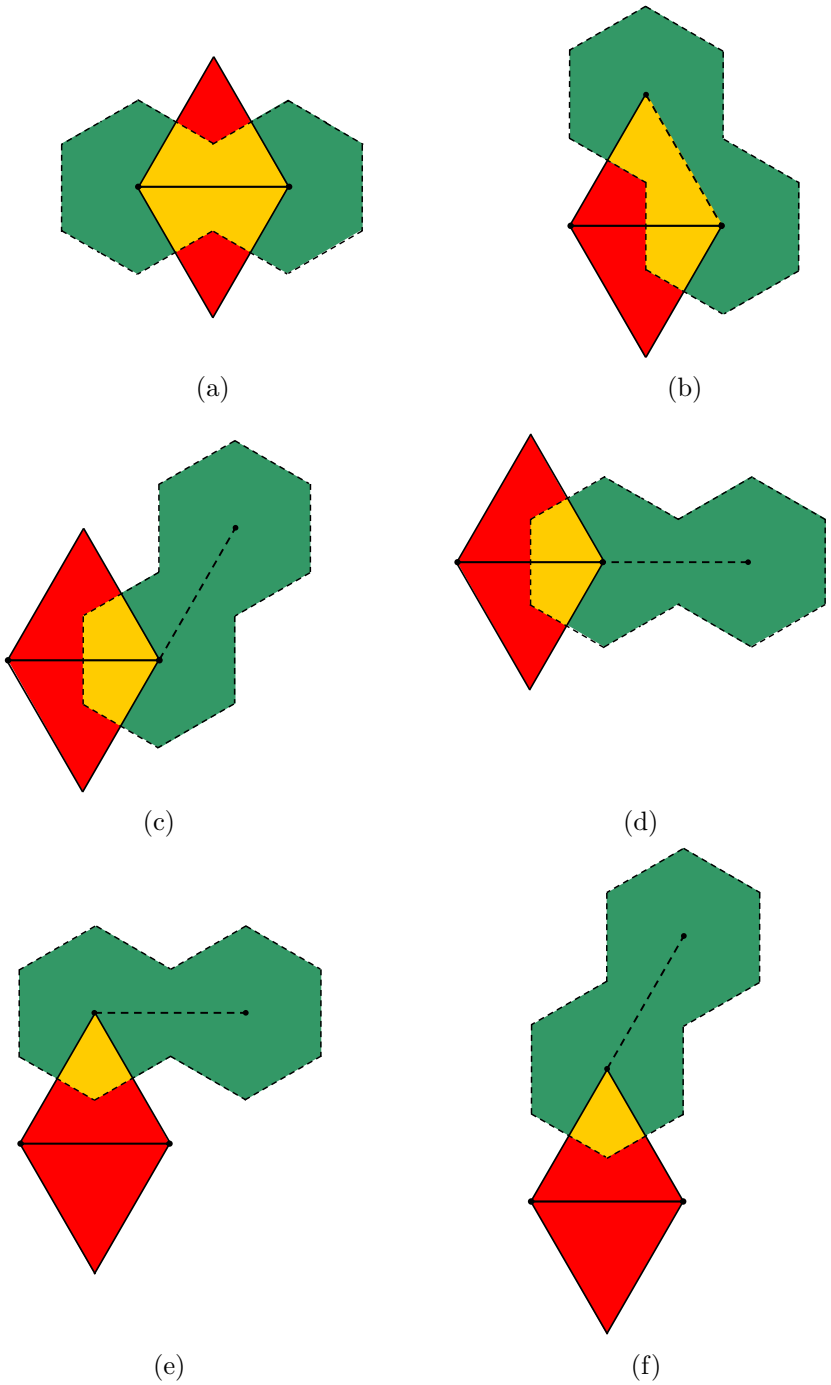

Figure 5.2: Testing of a RWG basis function with a $\hat{\boldsymbol{n}}\times$ BC testing function. The basis function is shown in red, the testing function is shown in green, and their intersection, where the inner product (test) is actually carried out, is shown in yellow. The different cases provide (a) 1, (b) 4, (c) 4, (d) 2, (e) 4, and (f) 4 constraint conditions (measurements) to the basis function, respectively.

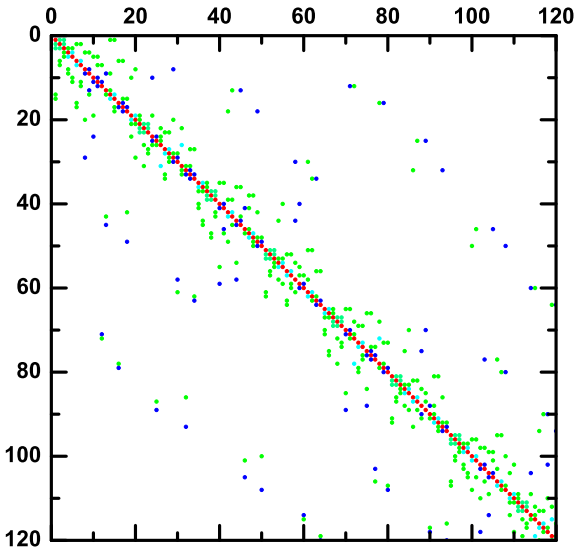

(a)

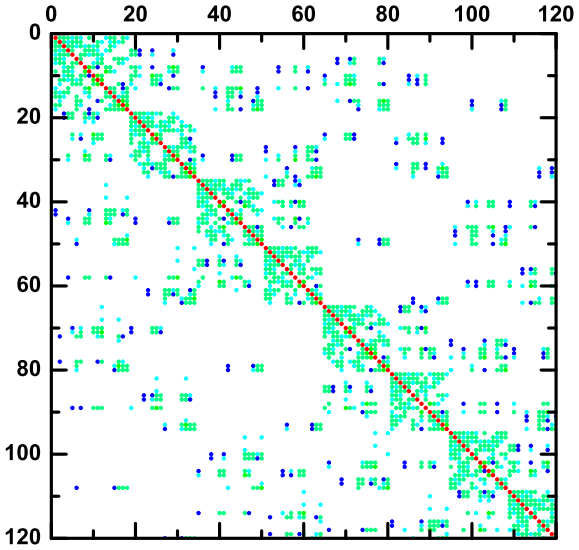

(b)

Figure 5.3: Sparse patterns of the system matrices obtained by discretizing the identity operator using (a) RWG and (b) $\hat{\boldsymbol{n}}\times$ BC as testing function. Different constraint intensities are indicated with different colors.

CHAPTER 6

CONCLUSION

In this thesis, the surface integral equations that are widely used in computational electromagnetics are investigated as the Fredholm integral equations of the first and the second kind. The mathematical characteristics of the operators involved in these integral equations are discussed and the corresponding discretization strategies are studied. The rotated BC function is shown, both theoretically and numerically, to be a better testing function for the discretization of the second-kind integral equations for both the PEC and the dielectric cases. It is demonstrated through some numerical experiments that by using the presented discretization scheme, the discretization error of the identity operator, which is shown to be a major error source of the second-kind integral equations, can be suppressed significantly.

A near-singularity extraction technique is presented and applied for both the $\mathcal{K}$ and the $\mathcal{T}$ operators, in order to reduce the numerical error in the evaluation of the system matrix elements. To measure the numerical errors in the solution of generally shaped objects accurately, the null-field problems are presented and the RMS of the total electric field in the far-zone is defined as the numerical error according to the extinction theorem. It has been shown, from the numerical examples in both the PEC and the dielectric cases, that the proposed techniques are able to reduce the numerical errors of the second-kind integral equations significantly, leading to accurate numerical solutions that are comparable to (or even better than) the existing solutions of their first-kind counterparts in solving problems with generally shaped objects.

At the same time, the fast convergence of the second-kind integral equations are maintained with the rotated-BC testing scheme. In the PEC case, the CFIE with a mixed discretization scheme is proposed to eliminate the spurious interior resonance corruption, and the optimal choice of the combination factor is shown to be around 0.2 to 0.3. In the dielectric case, the proposed rotated-BC testing scheme maintains the immunity of the spurious

interior resonance corruption of the Müller equations, leading to an accurate and fast convergent formulation at all frequencies.

It is also shown that the proposed discretization scheme can be regarded as an implicit Rayleigh-Ritz scheme, which is able to minimize the system energy and stabilize the numerical solution. The reason for the accuracy improvement is also discussed in terms of the method of weighted residuals. Several important concluding remarks related to the accuracy issue of the second-kind integral equations are made.

REFERENCES

[1] C. T. Tai, *Dyadic Green Functions in Electromagnetic Theory*, 2nd ed. Piscataway, NJ: IEEE Press, 1994.

[2] E. I. Fredholm, "Sur une classe d'equations fonctionnelles," *Acta Mathematica*, vol. 27, pp. 365–390, 1903.

[3] J. R. Mautz and R. F. Harrington, "H-field, E-field, and combined-field solutions for conducting bodies of revolution," *Arch. Elektron. Ubertragungstech. (Electron. Commun.)*, vol. 32, no. 4, pp. 159–164, 1978.

[4] A. J. Poggio and E. K. Miller, "Integral equation solutions of three dimensional scattering problems," in *Computer Techniques for Electromagnetics*, R. Mittra, Ed. Elmsford, NY: Permagon, 1973.

[5] Y. Chang and R. Harrington, "A surface formulation for characteristic modes of material bodies," *IEEE Trans. Antennas Propag.*, vol. 25, no. 6, pp. 789–795, June 1977.

[6] T.-K. Wu and L. L. Tsai, "Scattering from arbitrarily-shaped lossy dielectric bodies of revolution," *Radio Sci.*, vol. 12, no. 5, pp. 709–718, 1977.

[7] S. Yan, J.-M. Jin, and Z. Nie, "A comparative study of Calderón preconditioners for PMCHWT equations," *IEEE Trans. Antennas Propag.*, vol. 58, no. 7, pp. 2375–2383, July 2010.

[8] C. Müller, *Foundations of the Mathematical Theory of Electromagnetic Waves*. Berlin, Germany: Springer, 1969.

[9] P. Ylä-Oijala and M. Taskinen, "Well-conditioned Müller formulation for electromagnetic scattering by dielectric objects," *IEEE Trans. Antennas Propag.*, vol. 53, no. 10, pp. 3316–3323, Oct. 2005.

[10] S. Yan, J.-M. Jin, and Z. Nie, "Calderón preconditioner: From EFIE and MFIE to N-Müller equations," *IEEE Trans. Antennas Propag.*, vol. 58, no. 12, pp. 4105–4110, Dec. 2010.

[11] J. M. Rius, E. Úbeda, and J. Parrón, "On the testing of the magnetic field integral equation with RWG basis functions in method of moments," *IEEE Trans. Antennas Propag.*, vol. 49, no. 11, pp. 1550–1553, Nov. 2001.

[12] E. Úbeda and J. M. Rius, "MFIE MoM-formulation with curl-conforming basis functions and accurate kernel-integration in the analysis of perfectly conducting sharp-edged objects," *Microw. Opt. Technol. Lett.*, vol. 44, no. 4, pp. 354–358, Feb. 2005.

[13] E. Úbeda, A. Heldring, and J. M. Rius, "Accurate computation of the impedance elements of the magnetic-field integral equation with RWG basis functions through field-domain and source-domain integral swapping," *Microw. Opt. Technol. Lett.*, vol. 49, no. 3, pp. 709–712, Mar. 2007.

[14] L. Gürel and Ö. Ergül, "Singularity of the magnetic-field integral equation and its extraction," *IEEE Antennas Wireless Propag. Lett.*, vol. 4, pp. 229–232, 2005.

[15] Ö. Ergül and L. Gürel, "Improved testing of the magnetic-field integral equation," *IEEE Antennas Wireless Propag. Lett.*, vol. 15, pp. 615–617, 2005.

[16] Ö. Ergül and L. Gürel, "Solid-angle factor in the magnetic-field integral equation," *Microw. Opt. Technol. Lett.*, vol. 45, no. 5, pp. 452–456, June 2005.

[17] Ö. Ergül and L. Gürel, "Improving the accuracy of the MFIE with the choice of basis functions," in *2004 IEEE AP-S Int. Symp. and URSI Radio Sci. Mtg.*, Monterey, CA, June 2004, pp. 3389–3392.

[18] Ö. Ergül and L. Gürel, "Improving the accuracy of the magnetic field integral equation with the linear-linear basis functions," *Radio Sci.*, vol. 41, pp. 1–15, 2006.

[19] Ö. Ergül and L. Gürel, "Linear-linear basis functions for MLFMA solutions of magnetic-field and combined-field integral equations," *IEEE Trans. Antennas Propag.*, vol. 55, no. 4, pp. 1103–1110, Apr. 2007.

[20] P. Ylä-Oijala, M. Taskinen, and S. Järvenpää, "Analysis of surface integral equations in electromagnetic scattering and radiation problems," *Engineering Analysis with Boundary Elements*, vol. 32, no. 3, pp. 196–209, 2008.

[21] S. Yan and Z. Nie, "On the Rayleigh-Ritz scheme of 3D MFIE and its normal solution," in *Proc. IEEE Antennas Propag. Symp.*, San Diego, California, USA, July 2008.

[22] Ö. Ergül and L. Gürel, "Discretization error due to the identity operator in surface integral equations," *Computer Physics Communications*, vol. 180, no. 10, pp. 1746–1752, Oct. 2009.

[23] C. P. Davis and K. F. Warnick, "High-order convergence with a low-order discretization of the 2-D MFIE," *IEEE Antennas Wireless Propag. Lett.*, vol. 3, no. 1, pp. 355–358, 2004.

[24] K. F. Warnick and A. F. Peterson, "3D MFIE accuracy improvement using regularization," in *Proceedings of IEEE Antennas and Propagation Society International Symposium*, Honolulu, HI, June 2007, pp. 4857–4860.

[25] A. Buffa and S. H. Christiansen, "A dual finite element complex on the barycentric refinement," *Mathematics of Computation*, vol. 76, no. 260, pp. 1743–1769, Oct. 2007.

[26] K. Cools, F. P. Andriulli, F. Olyslager, and E. Michielssen, "Improving the MFIE's accuracy by using a mixed discretization," in *Proc. IEEE Antennas Propag. Symp.*, North Charleston, SC, June 2009.

[27] W. C. Chew, C. P. Davis, K. F. Warnick, Z. P. Nie, J. Hu, S. Yan, and L. Gürel, "EFIE and MFIE, why the difference?" in *Proc. IEEE Antennas Propag. Symp.*, San Diego, California, USA, July 2008.

[28] S. Yan, J.-M. Jin, and Z. Nie, "Implementation of the Calderón multiplicative preconditioner for the EFIE solution with curvilinear triangular patches," in *Proc. IEEE Antennas Propag. Symp.*, North Charleston, SC, June 2009.

[29] B. A. Finlayson and L. E. Serven, "The method of weighted residuals—a review," *Applied Mechanics Review*, vol. 19, no. 9, pp. 735–748, 1966.

[30] C. A. Balanis, *Advanced Engineering Electromagnetics*. New York: Wiley, 1989.

[31] J.-M. Jin, *Theory and Computation of Electromagnetic Fields*. Hoboken, NJ: Wiley, 2010.

[32] A. F. Peterson, "The "interior resonance" problem associated with surface integral equations of electromagnetics: Numerical consequences and a survey of remedies," *Electromagnetics*, vol. 10, no. 3, pp. 293–312, 1990.

[33] G. C. Hsiao and R. E. Kleinman, "Mathematical foundations for error estimation in numerical solutions of integral equations in electromagnetics," *IEEE Trans. Antennas Propag.*, vol. 45, no. 3, pp. 316–328, Mar. 1997.

[34] L. Gürel and Ö. Ergül, "Contamination of the accuracy of the combined-field integral equation with the discretization error of the magnetic-field integral equation," *IEEE Trans. Antennas Propag.*, vol. 57, no. 9, pp. 2650–2657, Sep. 2009.

[35] P. Ylä-Oijala and M. Taskinen, "Calculation of CFIE impedance matrix elements with RWG and $\hat{\boldsymbol{n}}\times$RWG functions," *IEEE Trans. Antennas Propag.*, vol. 51, no. 8, pp. 1837–1846, Aug. 2003.

[36] X. Q. Sheng, J.-M. Jin, J. Song, W. C. Chew, and C.-C. Lu, "Solution of combined-field integral equation using multilevel fast multipole algorithm for scattering by homogeneous bodies," *IEEE Trans. Antennas Propag.*, vol. 46, no. 11, pp. 1718–1726, Nov. 1998.

[37] P. Ylä-Oijala and M. Taskinen, "A novel combined field integral equation formulation for solving electromagnetic scattering by dielectric and composite objects," in *Proc. IEEE Antennas Propag. Symp.*, vol. 4B, July 2005, pp. 297–300.

[38] M. S. Yeung, "Single integral equation for electromagnetic scattering by three-dimensional homogeneous dielectric objects," *IEEE Trans. Antennas Propag.*, vol. 47, no. 10, pp. 1615–1622, Oct. 1999.

[39] S. Yan and Z. Nie, "A set of novel surface integral equations for electromagnetic scattering from homogeneous penetrable objects," in *Asia-Pacific Microwave Conference*, Hong Kong, China, Dec. 2008.

[40] S. M. Rao, D. R. Wilton, and A. W. Glisson, "Electromagnetic scattering by surfaces of arbitrary shape," *IEEE Trans. Antennas Propag.*, vol. 30, no. 3, pp. 409–418, May 1982.

[41] R. D. Graglia, D. R. Wilton, and A. F. Peterson, "Higher order interpolatory vector bases for computational electromagnetics," *IEEE Trans. Antennas Propag.*, vol. 45, no. 3, pp. 329–342, Mar. 1997.

[42] F. P. Andriulli, K. Cools, H. Bağci, F. Olyslager, A. Buffa, S. Christiansen, and E. Michielssen, "A multiplicative Calderón preconditioner for the electric field integral equation," *IEEE Trans. Antennas Propag.*, vol. 56, no. 8, pp. 2398–2412, Aug. 2008.

[43] S. Yan, J.-M. Jin, and Z. Nie, "EFIE analysis of low-frequency problems with loop-star decomposition and Calderón multiplicative preconditioner," *IEEE Trans. Antennas Propag.*, vol. 58, no. 3, pp. 857–867, Mar. 2010.

[44] G. L. G. Sleijpen and D. R. Fokkema, "BiCGstab(l) for linear equations involving unsymmetric matrices with complex spectrum," *Electronic Trans. Numer. Anal.*, vol. 1, pp. 11–32, Sep. 1993.

[45] R. Barrett, M. Berry, T. F. Chan, J. Demmel, J. M. Donato, J. Dongarra, V. Eijkhout, R. Pozo, C. Romine, and H. V. der Vorst, *Templates for the Solution of Linear Systems: Building Blocks for Iterative Methods*. Philadelphia: SIAM, 1994.

[46] S. Yan, J.-M. Jin, and Z. Nie, "Improving the accuracy of the second-kind Fredholm integral equations by using the Buffa-Christiansen functions," *IEEE Trans. Antennas Propag.*, vol. 59, no. 4, pp. 1299–1310, Apr. 2011.

[47] M. G. Duffy, "Quadrature over a pyramid or cube of integrands with a singularity at a vertex," *SIAM J. Numer. Anal.*, vol. 19, pp. 1260–1262, 1982.

[48] R. D. Graglia, "On the numerical integration of the linear shape functions times the 3-D Green's function or its gradient on a plane triangle," *IEEE Trans. Antennas Propag.*, vol. 41, no. 10, pp. 1448–1455, Oct. 1993.

[49] W. C. Chew, *Waves and Fields in Inhomogeneous Media*. New York: IEEE Press, 1995.